Stacking and Their Boundaries in Few-layer Graphene: Stability and Electronic Properties in Bi- and Trilayer Graphene

PhD Thesis

Raúl Ignacio Guerrero Avilés

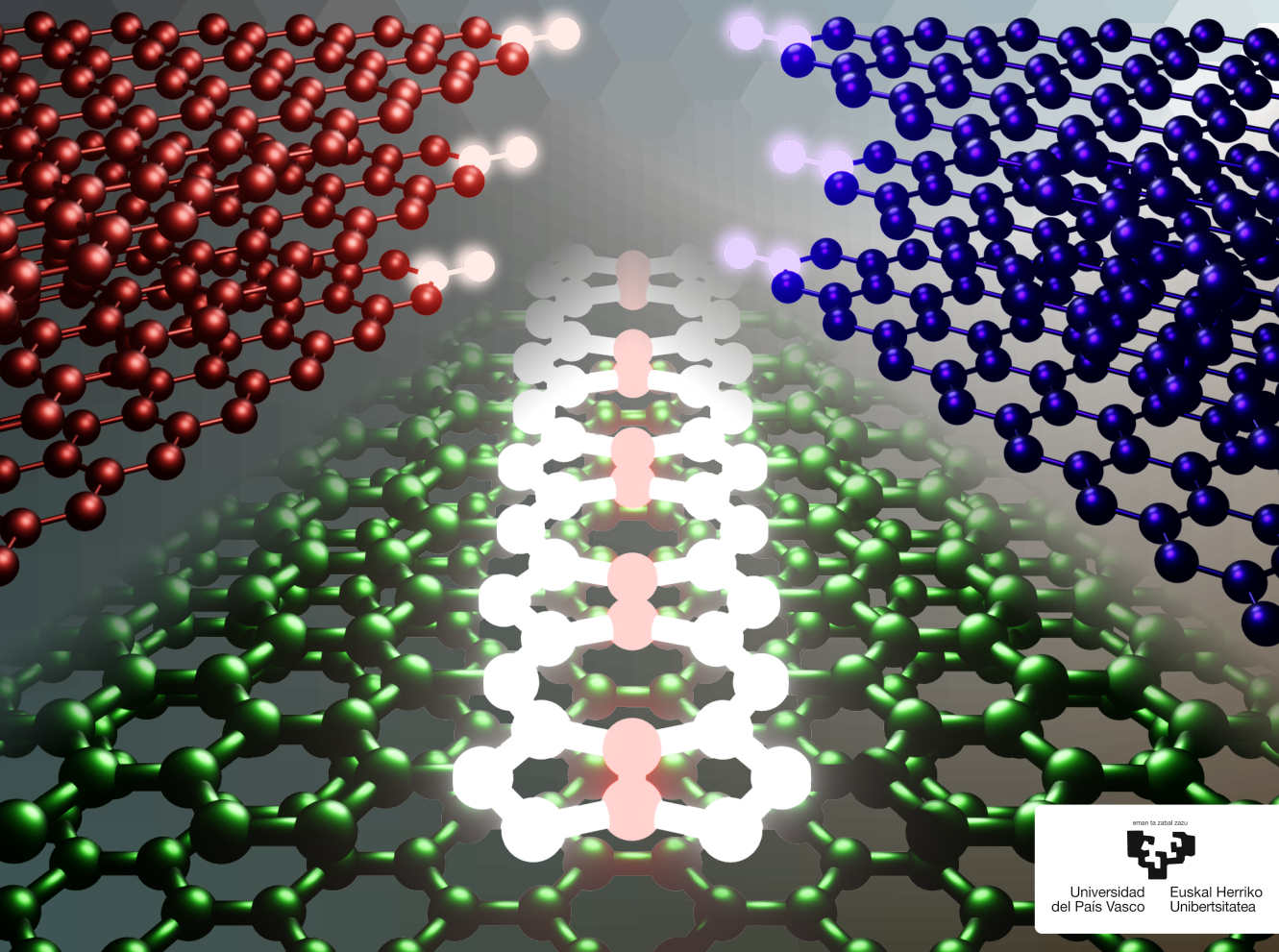

eman ta zabal zazu

Universidad del País Vasco

Euskal Herriko Unibertsitatea

Stackings and Their Boundaries in Few-Layer Graphene: Stability and Electronic Properties in Bi- and Trilayer Graphene

by

Raúl Ignacio Guerrero Avilés

A thesis presented for the degree of Doctor in Physics.
Universidad del País Vasco

Supervised by:

director
Andrés Ayuela Fernández

co-director
Marta Zuzanna Pelc

Department of Polymers and Advanced Materials:
Physics, Chemistry and Technology

eman ta zabal zazu

Universidad del País Vasco
Euskal Herriko Unibertsitatea

Donostia - San Sebastián, Spain.

Contents

List of Abbreviations

- AFM : atomic force microscope
- BLG : bilayer graphene
- BN : boron nitride
- BZ : Brillouin zone
- CNT : carbon nanotube
- GNR : graphene nanoribbon
- PMMA : poly(methyl methacrylate)
- SEM : scanning electron microscope
- STM : scanning tunneling microscope
- TLG : trilayer graphene
- ZGNR : zigzag graphene nanoribbon

List of Publications

Publications during the PhD period:

1 Raúl Guerrero-Avilés, Marta Pelc, Fabian R. Geisenhof, R. Thomas Weitz and Andrés Ayuela. Rhombohedral trilayer graphene is more stable than its Bernal counterpart. *Nanoscale*, 14:16295 2022.

2 Irene Casademont-Reig, Raúl Guerrero-Avilés, Eloy Ramos-Cordoba, Miquel Torrent-Sucarrat and Eduard Matito. How Aromatic Are Molecular Nanorings? The Case of a Six-Porphyrin Nanoring. *Angewandte Chemie International Edition*, 60: 24080, 2021.

3 Fabian R. Geisenhof, Felix Winterer, Stefan Wakolbinger, Tobias D. Gokus, Yasin C. Durmaz, Daniela Priesack, Jakob Lenz, Fritz Keilmann, Kenji Watanabe, Takashi Taniguchi, Raúl Guerrero-Avilés, Marta Pelc, Andrés Ayuela and R. Thomas Weitz. Anisotropic Strain-Induced Soliton Movement Changes Stacking Order and Band Structure of Graphene Multilayers: Implications for Charge Transport. *ACS Applied Nano Materials*, 2: 6067, 2019.

4 Raúl Guerrero-Avilés and Walter Orellana. Hydrogen storage on cation-decorated biphenylene carbon and nitrogenated holey graphene. *International Journal of Hydrogen Energy*, 43: 22966, 2018.

5 Raúl Guerrero-Avilés, Marta Pelc, Leonor Chico, W. Jaskólski and Andrés Ayuela. Periodic one-dimensional patterns on bilayer graphene: interplay between topological and defect states., *in preparation.*

Resumen

El uso de cálculos de primeros principios se ha vuelto crucial entre las diferentes disciplinas de la física de materia condensada. Permite predicciones del comportamiento de los materiales usando aproximaciones teóricas con bajo coste y sin necesidad de manipulación física. Una de estas aproximaciones es la teoría funcional de la densidad (DFT) la cual puede ser aplicada para sistemas lo suficientemente grandes y comparables con sistemas experimentales. Esta teoría encuentra el estado de mínima energía de un sistema electrónico al considerar todas las interacciones entre electrones y aproximando las interacciones de intercambio y correlación. En esta tesis, utilizamos DFT para estudiar las propiedades electrónicas de diferentes materiales bidimensionales basados en carbono.

En experimentos, el grafeno de pocas capas muestra propiedades electrónicas notables, pero para mantenerlas se requiere que se preserve el apilamiento durante todos los procesos. Sin embargo, los patrones de contactos metálicos y estampado de grafeno de pocas capas sobre nitruro de boro hexagonal (h-BN) puede llevar estiramientos anisotrópicos en las obleas de grafeno, lo que puede cambiar el orden de apilamiento en materiales bidimensionales tales como grafeno de tres capas. En la primera parte de esta tesis, examinamos la estabilidad relativa entre los órdenes de apilamiento romboédrico y Bernal en grafeno de tres capas ante diferentes deformaciones. Las deformaciones realizadas fueron estiramiento en el plano, compresión, cizallamiento y desplazamiento de las subredes de grafeno. Estas deformaciones nos permiten reproducir condiciones experimentales con el fin de compararlas con nuestros resultados y determinar las que inducen el cambio de apilamiento. Los resultados muestran que el apilamiento romboédrico es mas estable que el Bernal. Cuando inducimos deformaciones en el plano, notamos un cambio de apilamiento del romboédrico al

Bernal. Bajo compresiones grandes, el apilamiento romboédrico sufre una transición al Bernal. Compresiones pequeñas también pueden producir la estabilidad del apilamiento Bernal cuando el cizallamiento y el desplazamiento de las subredes conducen a anisotropías estructurales. Los resultados de cizallamiento se alinean con resultados experimentales previos en los cuales la deformación puede ser inducida por contactos metálicos, por el encapsulamiento entre otras capas de grafeno en muestras de h-BN, y al aplicar cizallamiento explícitamente en las muestras. Además, al desplazar subredes atómicas en grafeno de tres capas, la anisotropía estructural permite a estabilizar el apilamiento Bernal en ciertas direcciones. Los mecanismos de deformación como el cizallamiento y desplazamiento de subredes apuntan que la transición de apilamiento se puede lograr al romper la simetría de interacción entre capas en cada uno de ellos. Estos resultados indican que son posibles diferentes realizaciones prácticas, como el depósito de muestras en sustratos, y decoraciones con moléculas, donde pueden tener lugar las transiciones de apilamiento.

En la segunda parte, investigamos un arreglo de líneas de defecto en grafeno de dos capas hechas de octágonos y pentágonos. Dado que estas líneas de defecto han sido observadas experimentalmente, hemos hecho un patrón de estos defectos entre las capas que induce un cambio del apilamiento Bernal de AB a BA. La estructura electrónica muestra una interacción entre bandas relacionadas con estados topológicos y estados de las líneas de defecto. De hecho, las líneas de defecto muestran fases magnéticas con bloqueo espín-momento cuando se hibridan con estados topológicos. Observamos que los estados de defectos son susceptibles a campos magnéticos y dopaje n. Bajo campo eléctrico, el momento magnético con acople antiferromagnético tiende a ser ferromagnético. Luego, al aplicar dopaje tipo n al arreglo, las bandas de defecto se fijan al nivel de Fermi y están parcialmente ocupadas. Estas bandas muestran anidamiento para un dopaje igual a 1.0e. Los estados anidados corresponden a ondas de densidad de carga conmensuradas que se relacionan con inestabilidades de Peierls. Al aumentar el dopaje, los estados del bloqueo de espín-momento se ocupan. Cuando combinamos dopaje y valores grandes de campo, la estructura electrónica es dominada por el dopaje y el campo causa que las bandas de defecto se separen. De este modo, las líneas de defecto pueden ser utilizadas como canales de

conducción unidimensionales. Los resultados están a la espera de realizaciones experimentales con patrones de líneas de defecto, ya que nuestros resultados demuestran que los estados electrónicos en el arreglo de líneas de defecto pueden manipularse fácilmente.

Abstract

The use of first-principles calculations has become crucial in various fields of condensed matter physics. It allows for predictions of material behavior using theoretical approaches at a low cost and without the need for physical manipulation. One of such approach is density functional theory (DFT), which can be applied to systems large enough to be comparable to experimental ones. This theory finds the minimum energy state of an electronic system by considering all the interactions between electrons and approximating their exchange-correlation energy. In this thesis, DFT is used to study the electronic properties of two-dimensional carbon-based materials.

Experimentally, few-layer graphene exhibits exceptional electronic properties, but maintaining these properties requires preservation of the stacking throughout all processes. However, patterning of metal contacts and stamping few-layer graphene onto hexagonal boron nitride might can lead to anisotropic strains in graphene flakes, which can shift the stacking order in two-dimensional materials such as trilayer graphene. In the first part of this thesis, we examine the relative stability between rhombohedral and Bernal stacking orders in trilayer graphene under different deformations such as in-plane stretching, compression, shearing, and sublattice displacement. These deformations allow us to reproduce experimental conditions in order to compare them with our results and determine those that induce the stacking change. The results show that the rhombohedral stacking is more stable than the Bernal one. We induce in-plane deformations, we notice a stacking shift from rhombohedral to Bernal one, which agrees with experimental measurements. When large compressions are considered, the rhombohedral stacking suffers a transition to the Bernal one. Smaller compressions can also yield the Bernal stacking when shear and sublattice

displacement drive to structural anisotropies. The shear results are in line with previous experimental findings in which the deformation can be induced by metal contacts, by other encapsulating layered graphene within h-BN samples, and by explicitly putting shear on the samples. Furthermore, when shifting atomic sublattices in trilayer graphene, the structural anisotropy helps to stabilize the Bernal stacking in certain directions. Deformation mechanisms such as shear and sublattice displacement point out that the stacking transition is achieved by breaking the sublattice symmetries of the interlayer interactions involved in each stacking. These findings indicate that different practical realizations are possible, such as depositing samples in substrates, and molecule decoration, where stacking transitions may take place.

In the second part of this thesis, we investigate an array of defect lines in bilayer graphene made of pentagons and octagons. Because these defect lines have been observed experimentally, we pattern the defect lines between the layers inducing thus the change of the Bernal stacking from AB to BA. The electronic structure reveals an interplay between bands related to topological and defect-line states. In fact, the defect lines display magnetic phases with spin-momentum locking when they mix with topological states. We note that the defect states are affected by electric field and n-doping. Under electric field, the magnetic moment in the antiferromagnetic coupling tends to be as in the ferromagnetic case. Next, when we apply n-doping to the array, the defect bands are partially occupied and pinned at the Fermi level. They also are nested for n-doping value equal to 1.0e. The nested states correspond to a commensurate charge-density wave which could be related with Peierls instabilities. For larger n-doping values, the spin momentum locking states are filled. When we combine doping under large field values, the electronic structure is dominated by the n-doping and the field causes the defect bands to split. The defect lines in the array can thus be used as one-dimensional conducting channels. We are looking forward to experimental realizations that show the patterning of the defect lines, since our results show that the electronic states in the defect line array can be easily manipulated.

1 — Introduction

Material properties such as mechanical, thermal conductivity, and electronic ones have been, among others, a point to take into account by the scientific community. The first descriptions of materials were generally based on observations of their physical evolution under different external conditions. While most of those purely phenomenological conclusions were not clear from a fundamental point of view, these first conjectures paved the way for the development of modern science. In the nineteenth century, Michael Faraday described the current-temperature dependence of a thermo-resistant semiconductor like Ag_2S. In this experiment, Faraday used a simple lamp to heat Ag_2S and, with a galvanometer, realized that Ag_2S conductivity was thermo-dependent [1]. Nevertheless, Faraday's descriptions were phenomenological. Eventually, to understand these kinds of phenomena, the scientific community develop theories to reproduce them; although, it was not until the beginning of the twentieth century that Paul Drude developed the first classical theoretical model for electron conduction [2, 3]. We know nowadays that a quantum mechanical framework was still needed to explain the materials electronic behavior with better insight and accuracy. The first lights of quantum mechanics start around 1838 with Faraday's cathode ray experiments. From those days up to the early twentieth century, the scientific community suggested different hypotheses for quantum mechanical theory. In 1926 Erwin Schrödinger represented the atomic energy level quantization as an eigenvalue problem [4], in which he used the nowadays called Schrödinger's equation, that successfully reproduces the energy levels of hydrogen-like atoms. After Schrödinger contribution, the first quantum mechanic unification comes with Paul Dirac (with the Dirac equation for relativistic electrons [5]) and the John von Neumann mathematical for-

mulation [6, 7]. Subsequently, Walter Heitler and Fritz London proposed the first quantum mechanical approach for the covalent bond in hydrogen molecules [8]. After some decades, more theoretical descriptions appear, and in the 1960s Pierre Hohenberg and Walter Kohn formulated the two well-known Hohenberg-Kohn theorems [9], and Walter Kohn and Lu Sham articulated the Kohn-Sham ansatz [10, 11]. In those contributions, Kohn, Hohenberg and Sham use the Thomas-Fermi model to describe a simplified many-electron system with a Schrödinger-like equation. Thanks to that, we can describe the behavior of systems in a very efficient way allowing us to contrast theoretical and experimental results by working within density functional theory (DFT). Density functional theory provides the ground-state electron density, which considers the external interactions of an electronic system. In turn, it allows to predict material properties such as mechanical and electronic ones with enough precision. In addition, since DFT uses the electron density as a fundamental quantity, the numerical calculations require fewer computational resources when compared with wave-function-based theories.

Among the wide range of materials examined in the scientific literature, graphite is one of the most extensively studied by the scientific community, even nowadays. John Desmond Bernal (1924) studied graphite to characterize experimentally the stacking between the carbon layers [12, 13]. In those years, it was already known that graphite is composed of weakly coupled carbon layers. In the 1990s, experimentalists performed chemical deposition techniques to grow narrow graphite samples on metal surfaces [14]. Eventually, these experiments realized renewed methods to get thinner and thinner graphite samples until they finally obtained graphene. Among the different families of experimental methods reported to synthesize graphene there are the so-called top-down techniques, used in the 1970s [15]. One of those techniques is exfoliation by a scotch-tape, implemented by Ohashi et al. [16], in which they obtained about 30 graphene layers. At the beginning of the twenty-first century graphene was synthesized and identified. To separate one graphene layer from graphite, in 2004, Andre K. Geim and K. S. Novoselov also used the scotch-tape technique; this experiment gave them the 2010 Nobel prize in physics [17]. Graphene is the first two-dimensional crystal with one atom thickness. Its synthesis technique motivates several improvements in experimental

procedures like chemical vapor deposition (CVD) [18], plasma exfoliation [19], or mechanical cleavage from natural graphite samples [20]. Graphene unique electronic, mechanical and thermal properties make this material relevant to be studied [21]. For instance, when graphene is deposited on SiO_2, it reaches a thermal conductivity of $\kappa = 600$ W/(m·K) [22], which is even better than copper. Baradin *et al.* showed another remarkable result in 2008 in which they found that the thermal conductivity of free-standing graphene is about $4840 - 5000$ W/(m·K) [23]. Graphene has an optical absorption of 2.3% [24], and its identification is almost impossible with microscopy techniques like AFM or SEM [25]. Fortunately its light absorption makes it easy to be identified optically. Regarding the graphene stiffness, Bunch and coworkers estimated that graphene's Young modulus is around 1 TPa [26]. For example, it can be extrapolated to an elastic spring constant is around 39 N/m for a nm^2 monolayer. Hence, having graphene in small nanoscopic areas is quite stiff, while its stiffness promptly decreases when having large areas at the microscale. Graphene is a zero-gap semiconductor with high mobility carriers due to the linear band dispersion. Its electronic structure can be theoretically described using a Dirac Hamiltonian for simple massless particles. This Hamiltonian for $\pi-$electrons has two linear valence and conduction bands that accomodate to the so-called Dirac cones (or valleys). When graphene is isolated, its density of states is zero at the Fermi level, showing that it is electrically neutral and has minimum conductivity [27]. Nevertheless, graphene electronic properties can be easily tuned by being in contact with other materials, like substrates of SiO_2 or other 2D materials, impurities or even external conditions, which shift in energy the Dirac cones [28, 29, 30]. In fact, Bolotin and coworkers have shown that its conductivity improves in normal vacuum conditions and warming up graphene samples around 400 °C [31]. The Dirac cones host other remarkable properties such as anomalous diamagnetic susceptibility [32, 33], and half-integer quantum Hall effect [34, 35, 36]. Graphene properties can be hosted by graphene systems with few-layers, in which the physics behind graphene Dirac cones can be modified reaching effects like being semiconductor, van Hove singularities or even superconductivity.

Graphene allotropes, like nanoribbons and few-layered graphene, can inherit its incredible properties. The Bernal stacking in few-layered graphe

ne systems is currently known as the most common among other stackings. This statement comes from the fact that Bernal graphite is the most common in samples. Nevertheless, recent experiments undermine this statement [37] and demonstrate that Bernal graphite stability should not be extrapolated to few-layered graphene systems. Recent studies have reported few-layered graphene samples hosting several stacking orders [38, 39]. Transitions between these stacking orders might take place when adding patterned metallic contacts [38] inducing mechanical deformations, which change the electronic properties of the sample. In this context, mechanical deformations in samples with multiple stackings are interesting to be investigated because stacking transitions can occur and, consequently, change their related electronic properties. This is the case of trilayer graphene (TLG) samples in which domains with stacking order can change from rhombohedral (ABC) to Bernal (ABA). The rhombohedral trilayer graphene is a metastable phase [40] that differs from the Bernal stacking in the third layer. It has nearly flat bands next to the Fermi level associated to tunable conducting surface states, while in the Bernal stacking the low energy bands show metallic behavior. Thus, transitions between these two stacking orders are of crucial importance when designing electronic devices. In the first project of this thesis, we examine the relative energy difference between the Bernal and rhombohedral trilayer graphene stackings under deformations. We deform the trilayer-graphene lattices and consecutively perform density functional theory calculations. During the calculations, we note different technical details which are related to relevant physics occurring at the graphene K (K′) points. We find that mechanical stretching induces rhombohedral to Bernal stacking transitions. Furthermore, we apply shear deformations and sublattice displacements which break the interlayer symmetries in the ABA and ABC stackings.

In the second collaboration, we focus on the electronic structure of bilayer graphene (BLG) with an array of grain boundaries. Each domain wall separates Bernal regions with opposite AB and BA stacking orders. We study an array of defect lines by using periodic boundary conditions. The periodicity causes the bilayer graphene band structure to open a gap that contains topologically protected states [41]. In fact, the effect of periodical stacking changes is also shown in works about twisted

bilayer graphene [42], in which even superconductivity is observed [43]. In addition, it has been recently shown that one-dimensional domain walls dominate the transport effects and host charge modulations in twisted bilayer graphene with small angles [44]. Our results study the electronic structure with spin polarization that drives to spin-momentum locking [45]. Furthermore, we consider the presence of charge modulations in the defect lines made of pentagons and octagons.

The thesis is organized as follows. We describe the density functional theory and a brief explanation of the most common exchange-correlation functionals in chapter 2. Next, we explain the linear response function for one-dimensional and quasi-one-dimensional systems. Because weak potentials can affect the response function and may modify the Fermi surface, we analyze the consequences of singularities and finite peaks in the response function regarding the nesting of bands. We later show that nested bands can be induced by charge modulation regimes so-called commensurate and incommensurate. In chapter 3, we show the motivation of our study on the relative stability of trilayer graphene phases, Bernal and rhombohedral, under mechanical deformations. Here, we describe both stacking phases and their electronic properties together with recent experimental facts in which such deformations may occur. The applied deformation are in-plane, out-of-plane, shear deformations and sublattice displacements, which are properly detailed in the chapter. Our theoretical results help to interpret experimental observations on trilayer and tetralayer graphene. They can advise establishing strategies to avoid or induce stacking transitions when patterning metal contacts in few-layered graphene samples with different stacking orders.

In chapter 4, we describe how extended grain boundaries affect the electronic structure of the most common monolayer and bilayer graphene allotropes. We focus on a specific grain boundary of pentagons and octagons (defect line), which has been experimentally obtained by Lahiri et al. [46]. We use this grain boundary to model an array of defect lines in bilayer graphene and then to study its electronic structure. We analyze the effects of electric fields and n-doping on the defect line array electronic structure. Note that by n-doping the defect line can show charge modulations. Finally, this thesis ends with the main conclusions about the results obtained. Supplementary information concerning Chaps. 3 and 4 can be

found in the Appendix.

2 — Theoretical Framework

2.1 Density Functional Theory

The many-electron problem considers an enormous number of interactions between electrons. As a consequence, there is a large number of variables, which makes this problem impossible to handle analytically and no exact solution can be obtained. Nevertheless, some numerical approximations yield particularly satisfactory results but with expensive computational costs. In contrast, density functional theory (DFT) is an approach to solve many-electron systems with a reasonable computational cost. This cost is reduced because it uses the electron density, n_0, rather than wavefunctions. The electron density is iterated in a self-consistent process based on the so-called Hohenberg-Kohn theorems to obtain the ground state electron density. On each self-consistent loop, DFT solves a Schrödinger-like equation for the electronic density. In many-electron systems, each electron interacts with other electrons in pairs, while in DFT each electron interacts with an effective density potential that comes from other electrons so that the complexity of the problem decreases. In other words, each electron interacts with a single potential derived from the electron density, which mimics the real electron system. In the following sections, we introduce the basic concepts and approaches that constitute DFT formalism.

2.1.1 Hohenberg-Kohn Theorems

The Hohenberg-Kohn theorems formalize the formulation of systems with multiple electron-electron interactions, like in the many-body problem. The Hamiltonian which represents the many-electron system is shown

as follows:

$$\hat{H} = \frac{\hbar^2}{2m_e}\sum_i \hat{\nabla}_i^2 + \sum_i \hat{V}_{ext}(\vec{r}_i) + \frac{1}{2}\sum_{i\neq j}\frac{e^2}{\left|\mathbf{r}_i - \mathbf{r}'_j\right|}, \tag{2.1}$$

where the first term is the kinetic energy ($\hat{T}$), followed by the external potential ($\hat{V}_{ext}$) and the Coulomb interaction between electrons. The $\hat{V}_{ext}(\mathbf{r})$ term includes the electron-nuclei interactions, and it can contain other external contributions like external electric fields.

To determine those terms and solve the main problem, Hohenberg-Kohn formulated two theorems[1]

Theorem 1 *For any system of interacting particles in an external potential $\hat{V}_{ext}(\mathbf{r})$, the potential $\hat{V}_{ext}(\mathbf{r})$ is determined uniquely, except for a constant, by the ground state particle density $n_0(\mathbf{r})$.*

Theorem 1 ensures that the potential $\hat{V}_{ext}(\mathbf{r})$ can be determined, but the ground-state density is still unknown. The second Hohenberg-Kohn theorem establishes that:

Theorem 2 *A universal functional for energy E[n] in terms of the density $n(\mathbf{r})$ can be defined, valid for an external potential $\hat{V}_{ext}(\mathbf{r})$. For any particular $\hat{V}_{ext}(\mathbf{r})$, the exact ground-state energy of the system is the global minimum value of this functional, and the density $n(\mathbf{r})$ that minimizes the functional is the exact ground state density $n_0(\mathbf{r})$.*

The second Hohenberg-Kohn theorem ensures that the energy functional can be defined by the electronic density and the ground-state density, n_0, minimizes the functional for a specific external potential.

Hohenberg-Kohn theorems yield the following density functional:

$$\hat{E}_{HK} = \hat{F}[n] + \int d^3r \hat{V}_{ext}(\mathbf{r})n(\mathbf{r}) + \hat{E}_{II}[n], \tag{2.2}$$

where the first term $\hat{F}[n]$ the so-called universal functional contains all the internal energies, such as kinetic and potential energies in the interacting electron system. The $\hat{E}_{II}[n]$ term is the repulsive ion-ion interaction,

[1] Taken from Reference [47].

where each ion can contain nuclei and core electrons. Because electronic systems are led by the valence electrons and not by cores nuclei, we usually consider that the close-shell electrons together with the nucleus constitute an effective core.

2.1.2 Hartree-Fock Approximation: Exchange Exact Solution

The wavefunction describing the many-electron system is antisymmetric even when the positions of two electrons are permuted. The Hartree-Fock method uses the variational principle to solve a Slater determinant as *ansatz* of the electronic system, preserving thus the wavefunction antisymmetry. This method ignores the effects of correlation between electrons and includes the exchange energies between them. The Hamiltonian representing the whole Hartree-fock system is $\hat{H}_{HF}$ and each element of it ($\hat{h}_{HF}$) operates on the Slater determinant orbitals ($\phi_i(\mathrm{r}_i)$), thus:

$$\hat{h}_{HF}\left|\phi_i(\mathbf{r}_i)\right\rangle = \left(\sum_{i=1}^{N} h_i + \frac{1}{2}\sum_{i=1}^{N}\sum_{i\neq j}^{N} J_{ij} - K_{ij}\right)\left|\phi_i(\mathbf{r}_i)\right\rangle, \tag{2.3}$$

where the first term, h_i, includes the single-electron and electron-nuclei energies. The J_{ij} and K_{ij} terms are the average Coulomb interaction between electrons - the so-called Hartree term- and the electron exchange energy, respectively. Considering orthonormal spin-orbitals and applying the variational principle, the Hartree and exchange terms are:

$$\hat{J}_{ij} = \int \frac{\left|\phi_j(\mathbf{r}_j)\right|^2}{|\mathbf{r}_j - \mathbf{r}'_i|} d\mathbf{r}_j, \tag{2.4}$$

and

$$\hat{K}_{ij} = \int \frac{\phi_j^*(\mathbf{r})\hat{P}_{ij}\phi_j(\mathbf{r}_j)}{|\mathbf{r}_j - \mathbf{r}'_i|} d\mathbf{r}_j, \tag{2.5}$$

with $\hat{P}_{ij}$ being the permutation operator between the *i-th* and *j-th* electrons. Then, the i-th electron interacts with other electrons, following the

expression

$$\hat{f}_i[\{\phi_j(\mathbf{r}_j)\}] = \hat{h}_i + \sum_{j=1}^{N} \hat{J}_i[\{\phi_j(\mathbf{r}_j)\}] - \hat{K}_i[\{\phi_j(\mathbf{r}_j)\}], \tag{2.6}$$

which is a functional of orbitals, the so-called *Fock operator*. Therefore, the Hartree-Fock Hamiltonian can be written as

$$\hat{H}_{HF} = \sum_{i=1}^{N} \hat{f}_i[\{\phi_j(\vec{r}_j)\}]. \tag{2.7}$$

The form of the Fock operator ensures that the self-interaction cancels exactly when $i = j$ in Eq. 2.6. This Hamiltonian operates on the Slater determinant, where the Fock operator provides an exact solution to the electronic system. The orbitals obtained are eigenstates of the Hartree-Fock Hamiltonian. The sum of the orbitals eigenvalues contributes directly to the total energy of the system. Because the exchange energy is included, the Hartree-Fock approximation provides a solution to the electronic system that ignores the correlation effects between electrons. The Hartree-Fock approximation considers the exchange energy between electrons, but unfortunately the total correlation energy is not included.

2.1.3 Kohn-Sham Method

Kohn and Sham formulate a self-consistent method that replaces the many-electron problem by an auxiliary independent-electron problem. They assume that the density of the many-electron system can be represented as in the case of independent particles. The Kohn-Sham Hamiltonian is

$$\hat{H}^{\sigma} = \hat{T}_s + V_{eff}^{\sigma}(\mathbf{r}), \tag{2.8}$$

where σ is the spin polarization. In the Kohn-Sham method, the non-interacting kinetic energy, $\hat{T}_s$, for N electron system is defined as:

$$\hat{T}_s = \frac{1}{2} \sum_{\sigma} \sum_{i=1}^{N_\sigma} \int d\mathbf{r} \left| \nabla \psi_i^{\sigma}(\mathbf{r}) \right|^2 .$$

The effective potential, V_{eff}, contains the Hartree interaction between electrons,

$$E_{Hartree}[n] = \frac{1}{2}\int d\mathbf{r}d\mathbf{r}'\frac{n(\mathbf{r})n(\mathbf{r}')}{|\mathbf{r}-\mathbf{r}'|}, \tag{2.9}$$

where the densities $n(\mathbf{r})$ is defined as sum of squares of the orbitals for each spin,

$$n(\mathbf{r}) \equiv \sum_{\sigma}\sum_{i=1}^{N_\sigma}\left|\psi_i^\sigma(\mathbf{r})\right|^2. \tag{2.10}$$

In addition the V_{eff} term also contains external interactions V_{ext}, i.e., the ion-ion interactions and the well known exchange-correlation functional E_{xc}. The Kohn-Sham functional is written as,

$$E_{KS}[n] = T_s[n] + \int d\mathbf{r}V_{ext}(\mathbf{r})n(\mathbf{r}) + E_{Hartree}[n] + E_{II}[n] + E_{xc}[n]. \tag{2.11}$$

This functional is minimized by the electron density, $\partial E_{KS}/\partial n = 0$, as expressed in the Hohenberg-Kohn second theorem. The last term of Eq. 2.11 corresponds to the exchange-correlation functional. The exchange-correlation functional it has no exact form and therefore it must be approximated. The LDA and GGA functionals are the early approximations for the exchange-correlation functional.

2.1.4 Exchange and Correlation Energies

The exchange-correlation functional contains fundamental information for predicting the electronic quantum interactions. Eventually, we can expand the exchange-correlation functional divided in exchange and correlation terms

$$E_{xc}[n] = E_x[n] + E_c[n].$$

Exchange. The exchange energy can be extracted from the Kohn-Sham approximation, this is,

$$E_x[n] = \langle E_{ee}[n]\rangle - E_{Hartree}[n]. \tag{2.12}$$

The first term is the electron-electron repulsion evaluated on the Kohn-Sham wavefunction. Note that by subtracting the Hartree term $E_{Hartree}$ from $\langle E_{ee}[n] \rangle$, we keep the unknown electron-electron interactions except the self-interaction ones. Therefore, if we consider a single electron system like a hydrogen atom the Eq. 2.3 and Eq. 2.12 will bring us to $E_x[n] = -E_{Hartree}[n]$ [48], canceling exactly the spurious Hartree interaction.

Correlation. The correlation energy shows us how much the behaviour of an electron is affected by the electronic distribution surrounding it. We can define the correlation energy as.

$$\begin{aligned} E_c[n] &= F[n] - T_s[n] - E_{Hartree}[n] - E_x[n] \\ &= T_c[n] + U_c[n] \end{aligned} \tag{2.13}$$

where $T_c[n]$ is the correlation term of the kinetic energy and $U_c[n]$ includes the non-kinetic ones. Thus the correlation energy for one-electron system is $E_c[n] = 0$. Below we describe the most common approximations of exchange-correlation functional to consider many electrons systems.

Local Density Approximation (LDA)

The local density approximation functional (LDA) is the basic approach for the exchange-correlation energy. It depends only of the electron density at each point of the space as follows,

$$E_{xc}[n] = \int n(\mathbf{r}) \epsilon_{xc}(n(\mathbf{r})) d\mathbf{r}, \tag{2.14}$$

where $\epsilon_{xc}(n(\mathbf{r}))$ is the exchange-correlation energy density. The integral in the exchange-correlation energy assumes that $\epsilon_{xc}(n(\mathbf{r}))$ evaluated at each point have the same density as in the homogeneous electron gas.

Although the LDA functional seems a preliminary approach to include the exchange-correlation energy, it has been used extensively. However, empirical (semi-empirical) corrections should be considered to reproduce the non-local electron behavior such as dispersion forces. For example, in the He_2 molecule, the LDA functional overestimates the binding en-

ergy and underestimates the interatomic distances [49]. These trends are systematic for all systems calculated within LDA functional.

General Gradient Approximation (GGA)

The general gradient approximation (GGA) is improving the predictions obtained by the LDA functional. Since real materials having inhomogeneous densities, more terms regarding the spatial density variation are considered. The GGA functional formulation also takes expansions of density gradients $|\nabla n(\mathbf{r})|$ to take into account the non-homogeneity of the true electron density. Unfortunately, such expansions truncate extensions and softness of the electron density when compared with the real density in materials [50]. The expression for GGA functionals is

$$E_{xc}^{GGA} = \int n(\mathbf{r}) \epsilon_x^{HEG} F_{xc}(n, |\nabla n|) d\mathbf{r}, \tag{2.15}$$

where ϵ_x is the exchange density for an independent-particle approximation. F_{xc} is a dimensionless term that is expanded in terms of $n(\mathbf{r})$ and its gradients, and its accuracy is still under improvement.

Nowadays, GGA functionals are between the most used by the DFT community, but they have some strengths and limitations. The limitations of the GGA results are no systematic trends and the underestimation of the gap in semiconductors. GGA functionals improves the lattice constant and bulk modulus predictions when compared to LDA, which are the reasons why it is being extensively used in the scientific community.

2.1.5 Dispersion Forces - Van der Waals Functionals

The dispersion forces are interactions between molecules or atoms that depend on much larger distances than the ones in covalent bonds. They are much weaker than covalent or ionic bonds, and govern systems based on dipole-dipole interactions. In the context of DFT, dispersion interactions are highly dependent on the electron correlation at a long range. In fact, they keep gaseous systems together like in the case of He dimer. Since He atoms are electrostatically neutral, the electron correlation is behind the bonding between He atoms. Because of the non-local characteristic of the dispersion forces, LDA and GGA functionals are not fully including those

forces in their formulations. In this sense, since LDA is a local functional and GGA truncates the densities with large ranges, non-local interactions must be explicitly included.

There are several ways in which the dispersion interactions can be included in the energy [51]. The London-like correction is the simplest one to include such interactions. This correction takes the form

$$E_{disp}^{London} = -\frac{C_6}{R_{AB}} f_{damp}(R_{AB}),$$

where C_6 is an empirical coefficient, R_{AB} is the distance between charge distribution, and f_{damp} is a damping function that avoids the short-range interactions [52, 53]. Unfortunately, because the empirical nature of this correction, it fails for systems when empirical coefficients are unknown.

Because different geometries and electron densities give different dispersion forces the development of these functionals is vast. Hence, there are several functionals improving the simulation of dispersion interactions. Examples are the vdw-DF2 (used in this thesis) and rev-vdw-DF2 functionals which are used for organic systems [54, 55]. These two functionals come from a method developed by Dion et al. that combines GGA and intra- and inter-molecular dispersion interactions [56]. The vdw-DF2 functional is applied to systems in which the electron density shows slow spatial variations like in solids. In this context, there is another functional developed by Hamada [55], the so-called rev-vdw-DF2, which is an extended version of vdw-DF2 to be applied to solids and molecular systems [57, 58].

2.2 Linear Response

The response function is related to how a system reacts to external influences such as electromagnetic fields, pressures or even geometrical deformations. In this section, we examine the case of a homogeneous electron gas under a weak and time-independent (static) external potential. The changes in the electron density, $\delta n(\mathbf{q})$, are related to the small changes of an *external potential*, $\delta v(\mathbf{q})$, following the expression

$$\delta n(\mathbf{q}) = \chi(\mathbf{q}) \delta v(\mathbf{q}), \tag{2.16}$$

where $\chi(\mathbf{q})$ is the response function. The density change in Eq. 2.16 can be specifically rewritten as follows

$$\delta n(\mathbf{q}) = \chi_s(\mathbf{q})\delta v_s(\mathbf{q}). \tag{2.17}$$

This expression – also called the Kohn-Sham theorem - contains the Kohn-Sham effective potential $\delta v_s(\mathbf{q})$ and the response function $\chi_s(\mathbf{q})$. Note that the $v_s(\mathbf{q})$ potential includes external contributions and exchange-correlation parts. The $\chi_s(\mathbf{q})$ term is the response function following the relation:

$$\chi_s(\mathbf{q}) = -\frac{k_F}{\pi^2}F(q/2k_F), \tag{2.18}$$

with $F(x)$ the Lindhard function, given as

$$F(x) = \frac{1}{2} + \frac{1-x^2}{4x} ln\left|\frac{1+x}{1-x}\right|. \tag{2.19}$$

The term $\delta v_s(\mathbf{q})$ in Eq. 2.17 has the following expression

$$\delta v_s(\mathbf{q}) = \frac{\delta v(\mathbf{q})}{\epsilon_s(\mathbf{q})}, \tag{2.20}$$

where

$$\epsilon_s(\mathbf{q}) = 1 - \frac{4\pi}{q^2}\left[1 - \gamma_{xc}(\mathbf{q})\left(\frac{\mathbf{q}}{2k_F}\right)^2\right]\chi_s(\mathbf{q}). \tag{2.21}$$

The term in the square bracket is the so-called local-field factor, and it is obtained from the linear response of a local field to an external one. We note that the slowly varying external potential δv is screened by the homogeneous electron gas in Eq. 2.20. In the long-wavelength regime ($\mathbf{q} \to 0$), Eq. 2.21 can be written as follows,

$$\epsilon_s(\mathbf{q} \to 0) = \frac{k_s^2}{\mathbf{q}^2}(q \to 0) + const., \tag{2.22}$$

where $k_s \approx \frac{1}{r_s^{1/2}}$ is the Thomas-Fermi screening length.

Using Eq. 2.16 and the Kohn-Sham theorem (Eq. 2.17) we now get

that

$$\chi(\mathbf{q}) = \frac{\chi_s(\mathbf{q})}{\epsilon_s(\mathbf{q})} = -\frac{k_F}{\pi^2}\frac{F(\mathbf{q}/k_F)}{\epsilon_s(\mathbf{q})}. \tag{2.23}$$

We have obtained an expression for the linear response function that depends on the eigenvalues and the Lindhard function. Because of screening, the resulting response function $\chi(q)$ is weaker than $\chi_s(\mathbf{q})$ by a factor depending on $\mathbf{q}^2/k_s^2$.

2.2.1 One-Dimensional Response Function

The response function depends on the dimensionality through the integration in the Brillouin zone. Nevertheless, it can be reduced to the Lindhard function shown in Eq. 2.19. Figure 2.1 shows a single-electron band. The red lines denote the linear electronic dispersion around the Fermi level, $\epsilon(k) - \epsilon(k+q) = \hbar v_F(k - k_F)$. When two states are separated

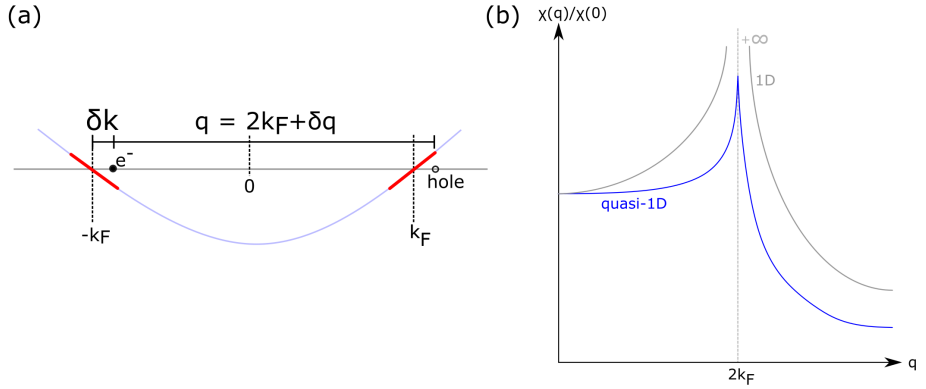

Figure 2.1: (a) Single electron band structure (blue curve). Red lines represent segments of the single electron band with linear character. (b) Response function corresponding to systems being one-dimensional (in gray) and quasi-one-dimensional (in blue).

by $q = 2k_F$ and have the same energy, we say that the band structure is *nested* in those states. When we introduce this vector in Eq. 2.19 a singularity appears at $\mathbf{q} = 2k_F$ as shown in the gray curve Figure 2.1. In fact, this peak is an effect of *perfect nesting* in the electronic structure of one-dimensional systems.

2.2.2 Quasi-One-Dimensional Case

Materials are not perfectly one-dimensional, for instance, material like carbon-nanotubes and graphene-nanoribbons are structures in which the electronic dispersions are quasi-one-dimensional. Other materials, like $NbSe_3$ or TaS_3, instead contain atomic "chains" extended in certain direction which interact between them. Depending on the strength of the interchain interaction, a quasi-one-dimensional behavior is induced in the Fermi surface of these materials. Their electronic dispersion is generally modeled by:

$$\epsilon(\mathbf{k}) = \epsilon_0 + \epsilon_x + \epsilon_y \tag{2.24}$$

$$= \epsilon_0 + 2t_x \cos(k_x a_x) + 2t_y \cos(k_y a_y), \tag{2.25}$$

with a_x being the lattice constant along the one-dimensional chain and a_y being the lattice constant perpendicular. The coupling between chains is t_y, and the intrachain one is t_x. In Fig. 2.2, we show the 2D electronic dispersion of Eq. 2.25 and how its Fermi surface changes due to the ratio between t_x and t_y. Panel (a) shows the case of $t_x = t_y$ in which the Fermi surface is nearly circular. Decreasing the interchain coupling t_y causes that the Fermi surface starts to deform [Figure 2.2(b)]. When we take the quasi-one-dimensional regime ($t_x \gg t_y$) and the same linear limit for the $\epsilon_x = v_F k$ term along the chain, Eq. 2.25 can be rewritten as follows

$$\epsilon(\mathbf{k}) = \epsilon_0 + v_F(k_x - k_F) + 2t_y \cos(k_y a_y). \tag{2.26}$$

The corresponding Fermi surface is displayed in Figure 2.2(c). This surface opens in two sinusoidal curves, a trend which is typical for quasi-one-dimensional systems. Note that we intentionally increase the periodicity of the model to show that the condition determining the Fermi surface shape of this system is due to the following expression, $k_x = k_F + \frac{2k_y}{v_F}\cos(k_y a_y) + O(2) + ...$, so that the Fermi surface has a sinusoidal shape. Finally, when the chains are fully uncoupled ($t_y = 0$), the Fermi surface has two straight lines, see Figure 2.2(d), just as described in the previous section.

Charge density waves. The Fermi nesting may drive to charge density

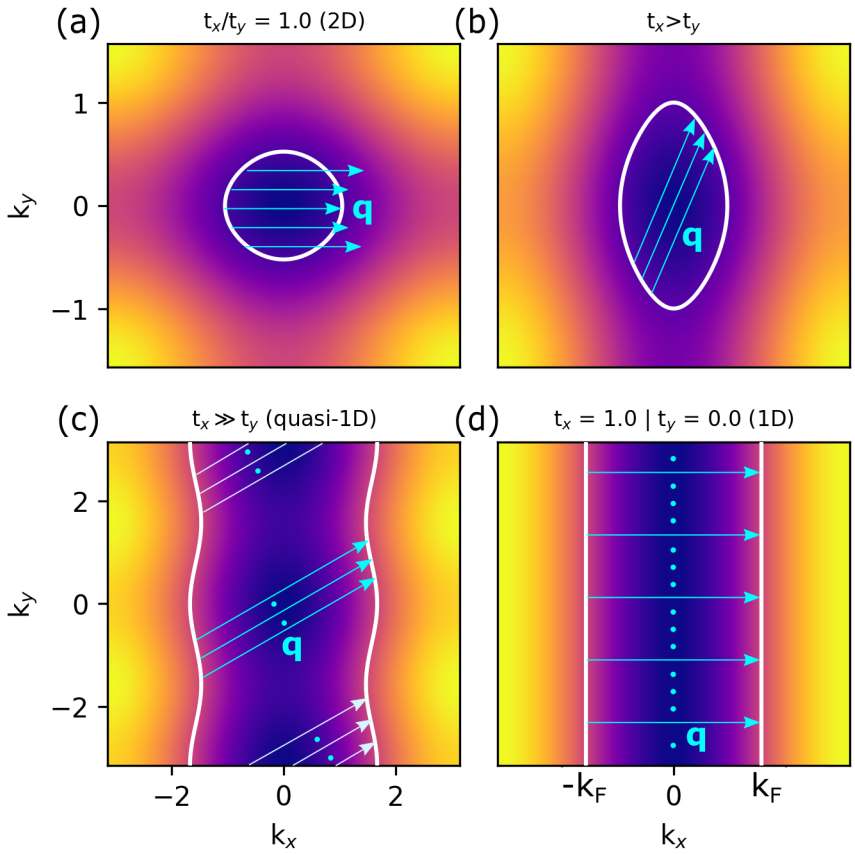

Figure 2.2: Fermi surface evolution of the single electron dispersion in Eq. 2.25 using different hopping ratios t_x/t_y. Panel (a) displays the case of $t_x = t_y$, which is a purely two dimensional system. Panel (b) shows the case of $t_x > t_y$ in which few sections have nested vectors. Panel (c) shows the quasi-one-dimensional case $t_x \gg t_y$; panel (d), the purely one-dimensional case, Arrows in cyan color represent the nesting vector, $\mathbf{q}$ and dots correspond to regions with the same nesting vector.

modulations, the so-called charge density waves (CDW). From Figure 2.2 it is easy to note the contribution at the nested regions of the Fermi surface. When eigenvalues are degenerated or nearly degenerated and separated by $\mathbf{q} \simeq 2k_F$, the Lindhard function and therefore the response function in Eq. 2.19 show an abrupt peak. In addition, because the system is two dimensional, the Fermi surface nesting may also occur between systems in which chains have a larger coupling factor, but with negligible consequences on the response function.

For these regimes, the CDW commensurability is given by

$$\lambda_0 = \frac{\pi}{k_F} = \frac{2\pi}{q} = \frac{N}{M} a_0, \tag{2.27}$$

where the N/M is the ratio of two integer values, and a_0 is the underlying lattice constant. When this ratio is a rational number the density modulation is commensurate with the underlying lattice, and it is incommensurate in the case of an irrational ratio. The CDW commensurability is a physical phenomenon in which the lattice periodicity changes, e.g., by atomic dimerization or trimerization. These distortions in the lattice cause Peierls instabilities which are related to metal-insulator transitions.

The study of the linear response function in a one-dimensional regime can be extrapolated to the quasi-one-dimensional case because both cases show an abrupt increase of the response function at $\mathbf{q} = 2k_F$. Regarding the nesting vector value, we expect a Peierls instability when $\mathbf{q} = 2k_F$. When having CDWs, the electron-phonon coupling could play an important role in low-dimensional metals. The nesting vector will define the periodicity of the CDWs, distortions of the underlying lattice and metal-insulator transitions, which define new phases to be experimentally observed when having finite temperatures.

3 — On the Relative Stability Between Trilayer Graphene Stackings

3.1 State of the Art

The stackings in graphite have been characterized since the first quarter of the last century [12]. In Figure 3.1 we show the Bernal stacking of graphite piling carbon layers, that graphene honeycomb lattices composed of the A (red) and B (blue) sublattices in its unitcell. Graphite layers are coupled due to van der Waals interactions. Multi and few-layered graphene

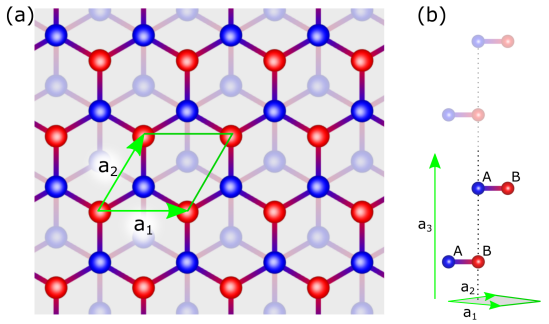

Figure 3.1: Graphite representation in Bernal staking order: (a) top view, and (b) side view. Blue and red colors represent the A and B sublattice atomic index.

stacking following the order in Fig. 3.1 is called Bernal. The stability of this stacking in graphite is usually extrapolated to multilayer graphene [59, 60]. Nevertheless, recent experimental results have shown that the

stability of Bernal stacking has to be revisited. For instance, trilayer graphene shows two stable stackings which can coexist in one sample as neighboring domains. The boundary between the domains can be in the form of corrugations or other defects, like being in strained samples due to other substructures [61, 38]. Experimental studies have shown that domains other than Bernal can be modified to end up in the Bernal stacking [62, 63]. Specifically, the transition from rhombohedral (ABC) to Bernal

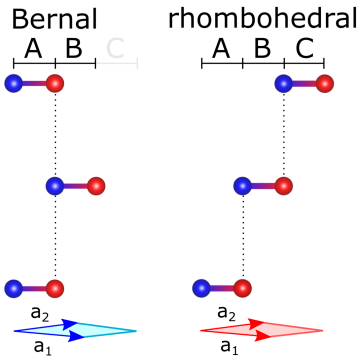

Figure 3.2: Unit cells of Bernal and rhombohedral stacked trilayer graphene.

(AB) stackings is found at temperatures above 1000 C°[64]. Other studies have shown that rhombohedral stacking can change to Bernal by evaporation of triazine molecules [65]. The transitions between the rhombohedral and Bernal domains start at the boundary formed by wrinkles or corrugations that slide when a driving force is applied. This displacement already suggests that mechanical deformations are crucial to study the stacking transitions between rhombohedral and Bernal domains.

The special interest in the stability of Bernal and rhombohedral trilayer graphene is related to their different electronic properties. Bernal trilayer-graphene have been extensively studied - as the one perceived as more stable and thus dominating in experimental samples showing metallic behavior [66]. The low-energy bands in this stacking are roughly a superposition of linear bands typical of graphene and bilayer graphene like-parabolic bands [67]. This band character stems from the mirror symmetry in this stacking. Unfortunately, when gating Bernal trilayer graphene, no gap is open because of the graphene-like linear band. The

parabolic bands are related to a "novel" quantum Hall effect due to chirality [68, 69], different than the one in monolayer graphene. The optical properties of AB-stacked graphene depend on the layer number and strength of the electric field applied [70, 71]. In the case of rhombohedral trilayer graphene, the low-energy bands follow a cubic behavior at the K point [72], where the bands become flat inducing Van Hove singularities in the density of states. Because of these flat regions, and therefore small electron velocities, electron-electron effects are expected to be important, with phenomena such as superconductivity [73, 74, 75] and magnetism [76].

Since the Bernal stacking has been considered more stable than the rhombohedral one and these stackings can coexist in the same experimental sample, we perform calculations for both stackings and show that the rhombohedral one has lower energy than its counterpart. We apply anisotropic and isotropic in-plane deformations as well as out-plane compression to determine the external conditions that cause Bernal stacking to be more stable. We also study lattice deformations like shear and sublattice displacements; these deformations can mimic experimental conditions that stacking transitions in experimental samples. For all studied deformations, we notice that the relative energy between the stackings depends on the deformation direction, and shows that external conditions are responsible for the stability of the Bernal stacking.

3.2 Computational Details

We perform density functional theory (DFT) calculations using the Viena *ab-initio* simulation package VASP [77, 78, 79]. This method based on plane waves is applied using a well converged kinetic energy cut-off of 700 eV. To represent accurately the relative energy difference between the Bernal and rhombohedral stacking, the cell volume is maintained equal in both cases. Because the energy difference between the Bernal and rhombohedral trilayer graphene stackings is well known to be small, the value of the electronic self-consistent tolerance is crucial to study such differences, which is set to 10^{-7} eV. For including dispersive interactions between layers, we use vdW-DF2 functional that improves the over-binding found LDA functional, when they are compared with non-routine Monte-

Carlo calculations for bilayer graphene [54, 80, 81]. Rigorous convergence tests in k-points, electronic relaxation, and comparison with other van der Waals functionals are included in Appendix A. To reproduce the trilayer graphene lattices we relax the cell shape keeping the unit cell volume constant, and fix the ions position in the xy plane while allowing them to move in the z direction. To describe the behavior of electrons near the Fermi level, we firstly perform our calculations using an smearing of 0.1 eV and a regular k-mesh grid of 30×30×1 being centered at Γ point. Because the relative stability between stacking orders seems to be a delicate issue, we improve the accuracy of our calculations by decreasing the smearing to 0.01 eV. The smearing is related to the k-mesh grid, and we set the mesh to 288×288×1 after performing the convergence tests. The k-mesh grids with values being multiple of three show a consistent trend in which the rhombohedral stacking is more stable. This difference between the two used k point samplings is required to reach energy differences in the order of $10^{-3} meV/nm^2$ and to include the nearly flat regions around K and K′ valleys when the lattices are deformed. These regions contain the relevant energy contributions where the low energy physics of multilayer graphene occurs.

3.3 Results

3.3.1 First Analysis and Experimental Approach

This section introduces the results of theoretical simulations on the different types of lattice deformations in the Bernal/rhombohedral trilayer graphene stackings. Experimental observations on few-layered graphene flakes have shown that different domains change their stacking order suggesting that mechanical deformations occur. We collaborate with the experimental group of Prof. Thomas Weitz from the Georg-August-Universität in Göttingen.

We published together a theoretical/experimental article that describes different deformations destabilizing the trilayer graphene phases and how to favor one stacking against the other. They exfoliate few-layer graphene samples in the order of 3 to 6 layers over different substrates to be patterned with metal contacts. Our theoretical results are focused on the

particular case of trilayer graphene because it is the minimal case having Bernal and rhombohedral stacking orders and shows the same behavior on samples containing more layers. We calculate the relative energy between the deformed lattices and compare our theoretical results with experimental observations. In this context, we show which stacking is more stable under deformations, and we help to understand why stacking changes occur in few-layered graphene samples. We define the relative energy difference as

$$\Delta E = \left(E_{aba} - E_{abc}\right)/S, \tag{3.1}$$

where S is the in-plane area of the unitcell. Note that the area varies concerning the deformation applied to the lattice.

Our first theoretical calculations show that the relative energy favors the rhombohedral stacking against its counterpart for undistorted lattices by 0.079 meV/atom. From this result, we begin our study by focusing on isotropic and anisotropic deformations. These deformations help us to understand whether the relative stability is direction dependent by applying strains in the armchair or zigzag direction of the graphene lattice. The isotropic deformation suggests that the homogeneous expansions maintain the rhombohedral stacking being more stable than the Bernal one, see Fig. 3.3. Therefore, we do not expect any change in the stackings from the experimental point of view. The experimental observation agrees with our calculations when the multilayer graphene sample is covered homogeneously with PMMA (Figure 3.3(b)), and when they exposed the sample to heating and subsequent cooling homogeneously inducing tension/compression of less than 1.6%.

For the anisotropic deformations of Fig. 3.3(a), we see that the energy of the rhombohedral stacking rises faster than in the case of the Bernal one. Then, the rhombohedral stacking can be destabilized more easily than the Bernal one, being the latter more stable under these deformations. When interpreting the experimental observations in Fig. 3.3(c), our collaborators note that the anisotropic deformations can occur while processing metal contacts on few-layered graphene flakes, which is also reported by Sanctis et al. [82]. During the process, the flake is heated up inducing its expansion and, after this, the metal contacts are deposited on the top of flake. This procedure clamps the regions of the flake below the contacts. Once the contacts are performed, the sample is cooled down, and

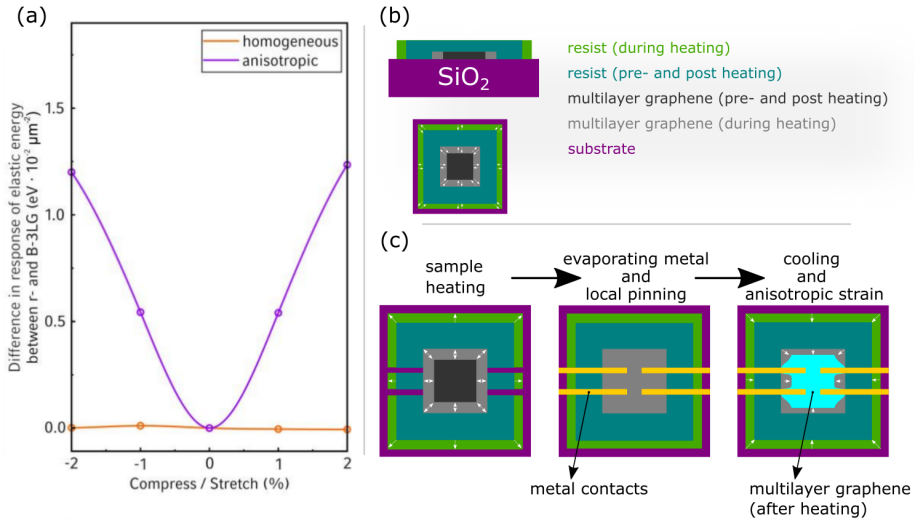

Figure 3.3: (a) Relative energy difference per unit area between Bernal and rhombohedral trilayer graphene for homogeneous and anisotropic deformations. (b) Schematic illustration of heating and cooling the sample covered with unpatterned resist leading to homogeneous deformation. (c) Proposed mechanism of how the combination of heating, local pinning during processing and subsequent cooling leads to anisotropic strain causing the preference of Bernal stacking. Left: the patterned resist heats up during evaporation and expands thermally, strechting the flake. Middle: The metal is forming a closed layer, locally pinning the flake in the hot state. Right: The resist cools down, contracting the flake in the nonpinned part of the flake thus inducing anisotropic strain in the flake. Panel (a) and (b) are extracted and modified from Ref. [38].

the non clamped regions shrink causing thus anisotropic strain, see right inset diagram in Fig. 3.3(c). The presence of shrunken and expanded regions whithin the sample and the presence of metallic contacts favor Bernal stacking, which agrees with our theoretical conclusions. Further experimental observations yield similar results when trilayer graphene is stamped on the h-BN substrate. After the stamping process, atomic force microscope experiments show that a contaminant layer between TLG layers is causing the appearance of several wrinkles and bumps in the flake, see Fig. 3.4(a, d). The experimental group then performed a cleaning pro-

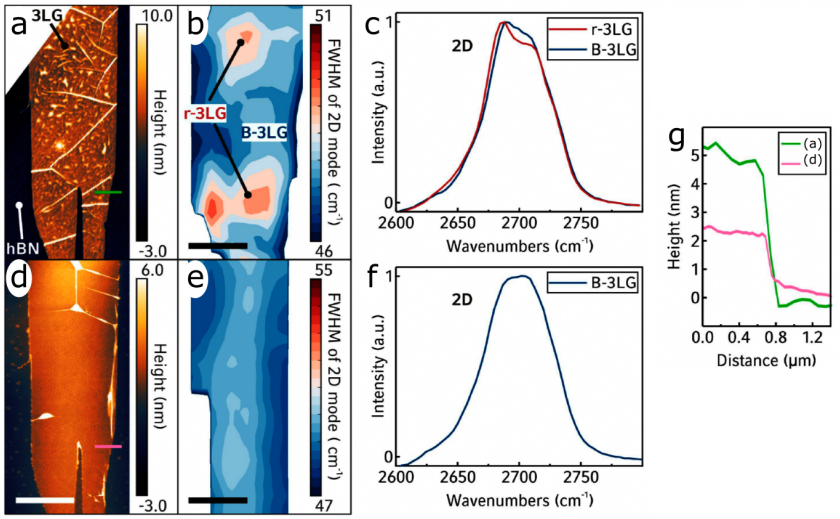

Figure 3.4: Soliton movement once the multilayer graphene is transferred in boron nitride h-BN substrate. Before the cleaning process: (a) atomic force microscope (AFM) image of the polymer stamping of graphene onto h-BN, (b) scanning Raman map of the 2D mode of the sample showing regions with Bernal (in blue) and rhombohedral (in red) trilayer graphene regions, and (c) 2D Raman peak showing both trilayer graphene stacking orders. After cleaning process: (d) AFM image showing loss of corrugations, (e) scanning Raman map of the 2D mode of the sample showing only Bernal stacking order, and (f) 2D Raman peak showing Bernal trilayer graphene. Panel (g) displays the green and red linecuts of the AFM images shown in (a) and (d) before and after the cleaning process, respectively. All the panels are from our Reference [38].

cess of the shown contaminant layer [83], that leads to the disappearance

of bumps and wrinkles, as shown in Fig. 3.4. The 2D Raman mode map shows that after the cleaning process, large areas of the rhombohedral stacking change to have the Bernal stacking, as shown by comparing panels (b) and (f). This observation is confirmed by looking at the 2D Raman mode peak of the Fig. 3.4(f) and (g). The transitions take place because the TLG regions are not simultaneously in close contact to the h-BN substrate during the cleaning process, inducing thus anisotropic strains that causes the resulting Bernal stacking.

3.3.2 Detailed Examination on Lattice Deformations

Since the stacking stabilities in trilayer graphene was found to be such delicate issue, we continued our simulations by improving the accuracy on our calculations, as detailed in Sec. 3.2, and expanding our analysis to study new deformations. After the computational parameters are set, we compare different functionals used for the Van-der-Waals-like dispersion energies. These functionals are key to reproduce the interactions between layers on graphene-like systems, and depending on the area of those layers the stacking order is found to be more stable as in experiments. It is interesting to see that for undistorted lattices, all tested van der Waals functional show that the rhombohedral trilayer graphene is more stable than the Bernal one.

Undistorted Stackings

We performed DFT simulations in order to calculate the relative energy between the stackings, as defined in Eq. 3.1. After setting the DFT parameters of Sec. 3.2, we relax the unitcell keeping their volumes equal for both stackings to ensure that the same plane-wave is used. The relaxation process shows that the carbon-carbon distance is $a_{c-c} = 1.43$ Å and the interlayer distance is d = 3.55 Å. Then, we used the relaxed geometries to display the band structure shown in Fig. 3.5 by performing single-point calculations along ΓKM path. The Bernal stacking band structure shows, as expected, a superposition of two parabolic-like bands confronting each other like in bilayer graphene, and two linear bands like in monolayer graphene. In fact, the low energy bands of the rhombohedral trilayer graphene electronic structure show a cubic behavior with a

small gap near the Fermi level which closes going along the KM path. We obtain a relative energy difference of 0.60 meV/nm^2 showing that the rhombohedral stacking is more stable than the Bernal one.

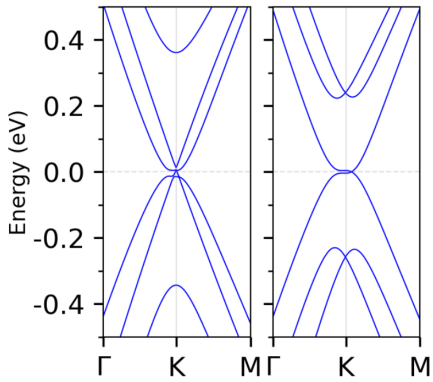

Figure 3.5: Electronic band structures for the Bernal (left) and rhombohedral (right) stacking of trilayer graphene.

In-plane Deformations

We study different in-plane lattice deformation by scaling its lattice vectors. First, we implement the homogeneous isotropic deformation described by $\vec{a}_{1,2} = \lambda(a_x\hat{i} + a_y\hat{j})$, where $a_{i,j}$ are the lattice vectors. This deformation causes a proportional lattice scaling with a constant interlayer distance. In this sense, when $\lambda = 1.0$ there is no strain and $\delta = 0\%$. We go up with strain to $\lambda = 1.05$; therefore, the δ strains are equal to 5%. Similarly, the compressions of $\lambda = 0.95$ are for $\delta = -5\%$. Figure 3.6(a) displays the total energy difference between the Bernal and rhombohedral stackings under homogeneous strains. The positive energy difference values (colored in red) are when the rhombohedral stacking is more stable than the Bernal one. Our results show that the Bernal stacking is relatively more stable than the rhombohedral one for strecking values around $\delta > 1.0\%$. Second, we consider the three anisotropic deformations: directional in zig-zag and armchair direction as well as area preserving deformations, as shown in Fig. 3.6(b). The armchair direction deformation follows the relation $\vec{a}_{1,2} = \lambda a_x\hat{i} + a_y\hat{j}$, while the deformations along zig-zag

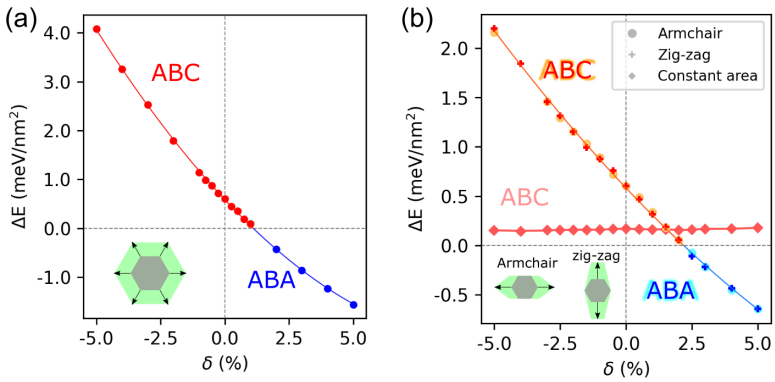

Figure 3.6: (a) Energy differences between Bernal and rhombohedral TLG versus in-plane homogeneous strains δ with compression (δ <0) and stretching (δ >0) in lattice parameters. (b) Energy differences for uniaxial deformations along zigzag and armchair directions. Blue-cyan and red-orange colors refer to the strain values when the Bernal and rhombohedral stackings are more stable, respectively. Energy differences are also given with strains assuming a constant area per nm^2 area, shown in light red. The insets in panels (a) and (b) indicate the homogeneous and uniaxial deformations in-plane, respectively. The TLG rhombohedral stacking is more stable even for small values of stretching, and a transition to the Bernal stacking is shown under expansions with $\delta \geq 1.0\%$ for homogeneous deformation. For anisotropic armchair deformations the transition is under $\delta \geq 2.0\%$.

direction follow $\vec{a}_{1,2} = a_x\hat{i} + \lambda a_y\hat{j}$. The constant area deformations have the relation $\vec{a}_{1,2} = \lambda a_x\hat{i} + a_y\hat{j}/\lambda$. In our results, the constant area deformation (Fig. 3.6(b)) shows that the rhombohedral stacking is more stable against the Bernal one for the whole range of δ values. Regarding the zig-zag and armchair deformations, we note that the energy differences are nearly overlaping. Both deformations show that the rhombohedral stacking is being more stable than the Bernal one until $\delta = 2.2\%$.

Figure 3.7 summarizes all the previous results. We note an asymmetry between transitions of the different deformations. These asymmetries occur within the experimental range; regarding the reversible strain attained for trilayer graphene samples in typical substrates [84]. Furthermore, strains beyond 1.0% could be artificially applied to graphene heterostructures [85], and strains till 0.3% have been seen in graphene layers encapsulated in h-BN [86].

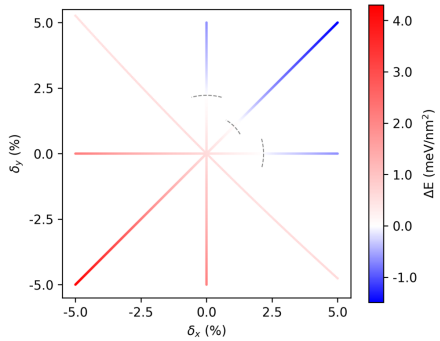

Figure 3.7: Summary of energy differences with respect to in-plane deformations δ_x and δ_y. Note the anisotropy of the rhombohedral-Bernal stability versus in-plane deformations.

Out-Plane Deformations

Next, we investigate out-plane deformations. The scaling factor ϵ changes the interlayer distance from its pristine value with $d = 3.55$ Å. With expansion, the rhombohedral stacking is being more favorable than the Bernal one even for interlayer distances up to d = 4.26 Å ($\epsilon = 20\%$) This compression shows that the Bernal stacking has lower energy than

the rhombohedral one for interlayer distances below 3.11 Å ($\epsilon < -2.5\%$). This result is in agreement with current calculations using vdW Grimme functional [87]. Transferring layers with the addition of protective layers

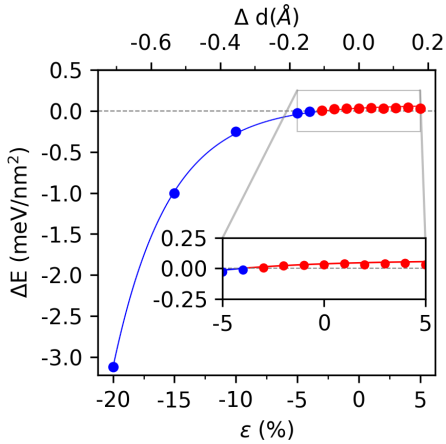

Figure 3.8: Out of plane deformations: total energy differences versus out of-plane strain ϵ related to the interlayer distance.

can induce compression on the few-layered graphene flakes causing Bernal stacking to be more stable. Since no stacking changes have been reported in procedures such as graphene encapsulation on h-BN [88], we can anticipate that TLG compressions can take place during these procedures. Furthermore, they can occur due to in-plane expansions of the sample. It is noteworthy that under constant volume, the compression of $\epsilon = -3.5\%$ corresponds to $\delta = 1.88\%$ of isotropic lattice expansion. In fact, the critical δ values for in-plane deformations reinforce that the transition to Bernal stacking happend when the samples are under compression.

Shear Strain Deformations

In the previous sections, the deformations preserve the interlayer symmetry; therefore, we analyze in this section the shear strain deformations to break it. The z-axis vector (a_3 lattice vector) drives the shearing process by azimuthal (ϕ) and polar (θ) angles, as shown in the top panels of

Fig. 3.9. The selection of the polar angle θ must maintains the interlayer nearest neighbors to preserve the Bernal and rhombohedral stackings that is true for angles below 15°, as shown in Fig. A.5 of Appendix A.

The lower panel of Figure 3.9 shows the energy differences per area between Bernal and rhombohedral stackings for the θ values of 10 and 5 degrees changing the ϕ angles up to 60°. The shear of $\theta = 10°$ induces an out-plane compression of ϵ = -1.5% while $\theta = 5°$ is compressing the interlayer distance to $\epsilon \sim -0.3$ %. These ϵ values are still well below the perpendicular strain distance to obtain the Bernal stacking, as shown in the previous section. Hence, the rhombohedral to Bernal stacking transition seems to be beyond the effects of the interlayer distance, but instead, it is a direct effect of applying shear deformations.

Note that using $\theta \neq 0°$, the shear displaces the layers in-plane, and with $\phi > 0°$ the top and bottom layers will describe cones relative to the middle layer. The displacement compels the p_z orbitals to change not only in the interlayer distance but also in angles, as shown in Fig. 3.9 top panels. On the one hand, the Bernal stacking energies present a 60° periodicity in ϕ while θ increases the amplitude of the relative energy difference. Therefore, the Bernal stacking is minimally affected up to $\phi = 30°$. On the other hand, the energies for the rhombohedral stacking show twice the Bernal stacking periodicity with 120° periodicity in ϕ. Thus, we find angles where the rhombohedral stacking is more destabilized than the Bernal. For the polar angles of $\theta = 5°$, the energy difference curve decreases within $\sim \pm 10.17$ meV/nm^2 as ϕ values increase. For the case of $\theta = 10°$, this energy range is $\sim \pm 75$ meV/nm^2, which is much larger than found in previously studied deformations. In fact, the energy differences are becoming an order of magnitude larger. For values of $\phi < 30°$, the rhombohedral stacking remains more favorable, while for values of $\phi > 30°$ we find that the Bernal stacking is stabilized more than the rhombohedral one. Comparing their symmetries, the Bernal stacking becomes more favorable for threefold directions $\phi = 60°$, see inset panel in Fig. 3.9. Interestingly, we observe a similar trend for $\theta = 5°$. The interlayer distance decreases for $\theta \neq 0$, which can play an important role in the relative energy difference, as shown in the previous section.

We set the interlayer distance like in the pristine case ($\epsilon = 0\%$) for $\theta = 10°$ to determine whether our results are depending on the polar angle

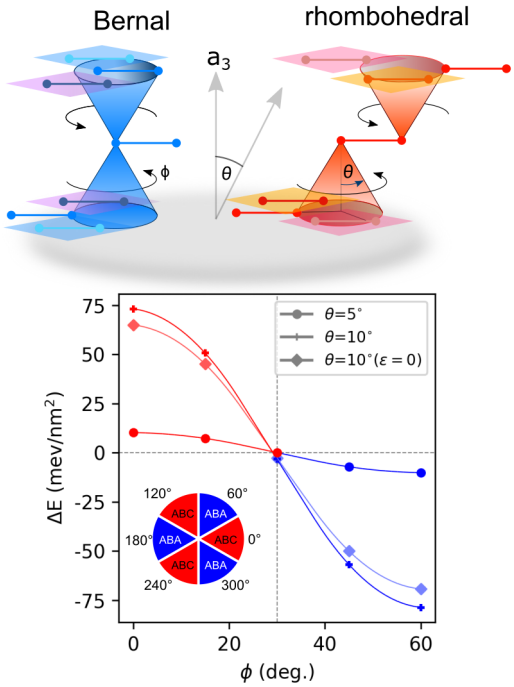

Figure 3.9: Stability energy difference between Bernal and rhombohedral stackings versus shear deformation, which is defined by angles θ and ϕ shown in the upper panel. The inset shows the shear ϕ for which the ABA and ABC stackings are more stable.

or the interlayer distance. The results confirm that the relative energy difference is mainly due to the shearing angle rather than the distance between layers. Although the energy differences decrease slightly, they remain in the order of tenths of meV/nm^2.

In general, the results for shear deformation depend on the ϕ angle to promote the Bernal or rhombohedral stacking. The shear deformation is crucial and can be used to control better the stability in electronic devices where the angle between layers is engineered [42].

Perpendicular Sublattice Displacements

In previous sections, the deformations change the layers in the same way without altering the sublattice positions in the cell. For completeness, we assess the role of out-plane sublattices anisotropy by displacing up and down the sublattices for each stacking. We now characterize how much the perpendicular shifting of the **A** or **B** sublattices affects the relative stability between Bernal and rhombohedral stackings. In this sense, we break the sublattice layer symmetry. First, when shifting up or down the middle layer on both stacking orders, their energy response does not exceed 0.01 meV, because both have the same number of interlayer neighbors. Therefore, we focus on its sublattices by analyzing the coordination number of carbon atoms between layers, i. e., the number of the first and second neighbors of each sublattice with the next layers.

Figure 3.10(a) shows the Bernal and rhombohedral stacking schemes indicating the second nearest neighbors in the next layers. The vertical lines from the middle layer sublattices indicate the first interlayer neighbors. The **A** and **B** type nodes have two first and 18 second neighbors belonging to the side layers in both stackings. However, the neighbor counting is different when looking to the top and bottom layers. In the case of Bernal stacking the middle sublattices neighbors are the same for the top and bottom layers because of its mirror symmetry. Thus, the shift yields the same energy because of Bernal stacking symmetry, i. e., which is independent of the shift direction. In the rhombohedral stacking, the middle layer neighbors for each sublattice site are "antisymmetric," i. e., shifting the **A** middle layer sublattice is equivalent to shifting down the **B** one – and in the opposite direction. For the rhombohedral geometry, the number of cases to discuss are two: (i) $\mathbf{A}_2^{\uparrow}$ (or to $\mathbf{B}_2^{\downarrow}$) and (ii) $\mathbf{A}_2^{\downarrow}$ (or $\mathbf{B}_2^{\uparrow}$),

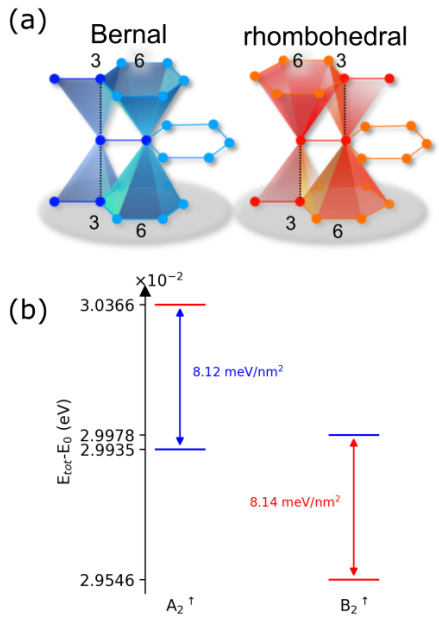

Figure 3.10: (a) Models for the Bernal and rhombohedral stacking including the number of interlayer nearest neighbors of the middle layer atoms, to be discussed in text. (b) Comparison of relative energies concerning the ground state of the perpendicular displacements of the $\mathbf{A}_2^{\updownarrow}$ and $\mathbf{B}_2^{\updownarrow}$ graphene sublattices in the middle layer. The subscript denotes the layer number, and the superscript arrow indicates the corresponding up and down shift of the sublattice atom.

where subscripts and arrows refer to the layer number and the direction of the out-plane displacement.

Figure 3.10 (b) compares the energy response difference, given as E_{tot}-E_0, where E_{tot} is the total energy when shifting the atoms and E_0 is the pristine ground state energy for each stacking. Shifting the atoms, by 1.0% of the pristine interlayer distance, about 0.034 Å, the total energy increases by ≈ 0.5 meV in all the considered cases. The energy response is nearly the same for the shifting cases of Bernal stacking. Contrary, the rhombohedral one shows a longer energy response; thus, moving the **A** sublattice up, $\mathbf{A}_2^{\uparrow}$, yields a different energy response than moving it downwards. As a result, moving $\mathbf{A}_2^{\uparrow}$ shows that the Bernal stacking is more stable than the rhombohedral one by 8.12 meV/nm2. By moving $\mathbf{B}_2^{\uparrow}$ (same as $\mathbf{A}_2^{\downarrow}$), the situation is just opposite, and the change of relative energy is about 8.1 meV/nm^2 – in this case, the Bernal stacking is more destabilized. These findings point out that the breaking between sublattice symmetries is another way to destabilize the stacking in the rhombohedral trilayer graphene.

Furthermore, these results might be explained by interpreting TLG stackings as trimers and dimers in the perpendicular direction. Here, the total energy can be written as a sum of eigenvalues and interatomic potentials with next-layer sublattices. Looking at the total contribution of interatomic potentials, the second interlayer neighbors cause the energy differences. This energy contribution adds to the difference in the sum of eigenvalues, already commented, in which the levels for the Bernal stacking split from the zero energy when the atoms are shifted up or down.

3.4 Conclusions

In this chapter, we determine when the Bernal stacking in trilayer-graphene becomes more stable than the rhombohedral one due to small lattice deformations. We compare the theoretical DFT calculations with experimental observations done by the group of Prof. Weitz. The experimental group observes that patterning of metal contacts and stamping few-layer graphene a onto h-BN substrate might cause anisotropic strains in the flakes. The strains induce the movement of stacking solitons in the rhombohedral Bernal boundaries that change the stacking order. Our re-

sults are surprising because a number of literature reports have contacted rhombohedral stacked multilayer graphene without reporting such transitions [89, 90, 91, 92, 93]. Metal contact fabrication can lead to lateral movements of Van-der Waals multilayers, which will also be potentially interesting for Van-der-Waals heterostructure design, when either lateral precision or twist angles are required [42].

In the second study of this chapter, we improve the accuracy of our calculations and study different lattice deformations, such as compression, shear and sublattice displacement. The rhombohedral stacking suffers a transition to the Bernal one when it is compressed below -2.5%. Smaller compressions can also yield the Bernal stacking when shear and sublattice displacement drive to structural anisotropies. These findings provide insights into the role of substrate-associated strains when graphene layers are integrated into devices. Thus, changing the stacking order modifies the electronic properties of few-layered graphene. Nowadays, experimentalists obtain the rhombohedral stacking by twisting and sliding the solitons between domain boundaries. Furthermore, by considering the anisotropic deformations, we claim that such deformations can cause a change of stacking, specifically by the stretching ones. Moreover, the shear results are in line with previous experimental findings in which the deformation can be induced by contacts [38], by other encapsulating layered graphenes within h-BN samples [37], and by explicitly putting shear on the samples [94]. These calculations raise further intriguing experiments regarding how substrates, molecules or nanoparticles, broke the sublattice symmetry on few-layered graphene heterostructures [95, 96]. In addition, the results in this chapter suggest that care must be taken when depositing exfoliated graphene on substrates and when top or edge contacts are patterned because of the strain forces in samples [82]. Trilayer graphene samples have to be analyzed once they are covered and isolated in operating devices to crosscheck whether regions with the rhombohedral stacking remain in the sample. Thus, this work would be interested in relevant technological areas such as patterning contacts and encapsulating graphene flakes in other materials.

4 — Electronic States of Grain Boundaries in Bilayer Graphene

In this chapter, we study the electronic structure in an array of pentagons-octagons (8-55) defect lines patterned in bilayer graphene (BLG). Firstly we review how the electronic structure of graphene changes when having grain boundaries, such as octagonal and 8-55 defect lines. Then we analyse the occurrence of topological states in its gap because gated bilayer graphene shows an energy gap in its band structure. These states can be induced from domain walls like electric field walls or stacking-domain walls separating the regions with AB-BA stacking domains. In this sense, 8-55 defect line and the topological boundary are the main ingredients to understand the physics behind the array of defect lines in bilayer graphene. We analyze the electronic structure of this array in detail by using simple-model, tight-binding and density functional theory simulations. We focus on the hybridization between the defect and topological states near the Fermi level. Because the electron-electron interaction seems to be crucial for their mixing, we perform DFT calculations to include magnetism and to study the different magnetic orders between the defect states in the array. Furthermore, we consider the array under external electric fields and n-doping also using DFT.

4.1 State of the Art

Many studies have reported domain walls separating the AB from BA domains in BLG [64, 97]. The domain walls can be corrugations or even

carbon substructures. In the minimal case of twisted bilayer graphene at very low angles, moire patterns have AB and BA domains separated by transition stacking domain walls. In this latter case, topologically protected states have been shown theoretically [98, 99] and experimentally [100]. Chou et al. also performed calculations to describe the presence of charge density waves along the domain wall of this system [44]. Additionally, it has been observed that twisted BLG host phenomena as unconventional superconductivity [42] which enhanced the efforts to investigate electron-electron correlated phenomena in other 2D materials. All these studies made an array of domain walls a good candidate for electronic devices design.

Octagonal/Pentagonal Grain Boundaries in Graphene

Synthesized graphene samples usually have grain boundaries in expe riments. Huang et al. grew monolayer graphene using chemical carbon deposition (CVD) techniques and found irregular grain boundaries (see Fig. 4.1(a)) [101]. A grain boundary in a hexagonal structure of graphene can be constituted of polygons, like pentagons, heptagons or octagons that separate two graphene domains rotated with respect to each other. Although they are found in irregular shapes, they can have nearly linear [102] or even linear configurations (Fig. 4.1(b)). For instance, Lahiri et al. performed scanning tunnelling microscope measurements and reported an 8-55 defect line, as shown in Fig. 4.2(a). They claim that this defect line can be used as quasi-one-dimensional metallic “wire” once its surrounding is doped. In this sense, these grain boundaries can be used as conducting channels interconnecting elements in device structures.

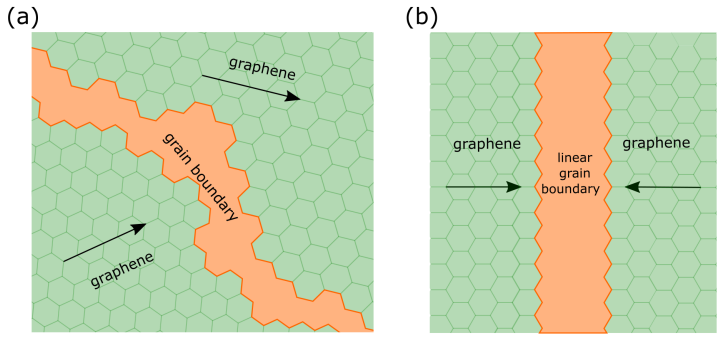

Figure 4.1: Schematic representation of an (a) irregular and (b) highly ordered grain boundary separating graphene domains.

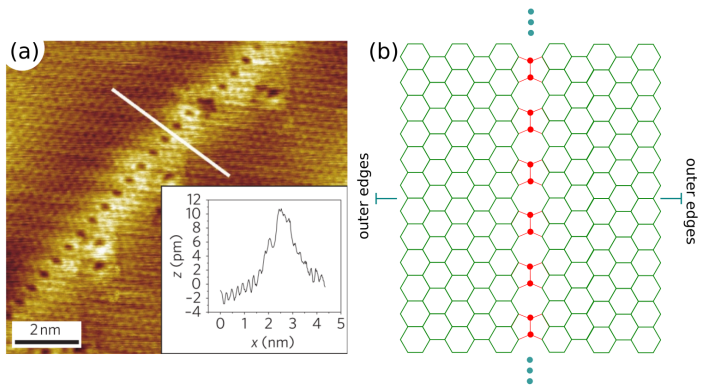

Figure 4.2: (a) Scanning tunneling microscope (STM) image of the defect line and profile perpendicular (inset). The brighter area corresponds to higher local density of states surrounding the defect. It originates from the states with wavefunctions localized in the line that decay exponentially inside the graphene regions. Experimental image obtained from Ref. [46]. (b) Schematic representation of the measured grain boundary composed of pentagons-octagons.

Grain boundaries in a zigzag graphene nanoribbon (ZGNR) like 8-55 defect lines can be used as conducting channel controlled by a gate voltage [103]. Because ZGNRs have an antiferromagnetic phase between its edges, the 8-55 defect line allows to manipulate the ZGNR polarization by stretching [104, 105]. Tight-binding calculations have been performed looking at an octagonal defect line embedded in a zigzag graphene nanoribbon [106]. The results (Fig. 4.3(b)) show that the curved bulk bands have a gap, which is typical of ZGNR [107]. In the gap, flat bands appear having different origins. At the Γ point (k = 0), two of these bands are located in the outer edges (Z_e) of the ZNGR, as shown in Fig. 4.3(c). When approaching the K point, these bands gain dispersion. At the Fermi level, there are also two degenerated flat bands. They are localized along the grain boundary when looking at the Γ point; see the K and Z_i wavefunctions. A state is located along the zigzag "edges" (Z_i) of the grain boundary; another mainly locates at the Klein node (K) and spreads into the graphene-like region. The Klein nodes of the octagonal defects can be next connected in pairs to get a pentagon-octagon defect line (Fig. 4.2(b)), and the states shift down in energy around -1.5 eV at the Γ point (Fig. 4.3(d)). There are left few flat bands at the zero-energy level, which get a dispersion near the K point. They are triple-degenerated, as expected, with two bands from the ZGNR outer edges. The remaining flat band state locates in the zigzag edges of the defect line when looking at its wavefunction at the Γ point (Z_i). We note that the defect-line state Z_i is robust and persists in the gap even when the Klein nodes are connected.

Then an armchair carbon nanotube with an 8-55 defect line is modeled (Figure 4.4). The previously shown 8-55 defected ZGNR along the armchair direction is rolled up, so that the coupling of the carbon outer edges results in their states to shift away from the Fermi level, as shown in Fig. 4.4(a). The Klein band thus changes its character connecting valence and conduction regions. When looking at the Γ point, the states at the Fermi level are still located at the zigzag edges of the defect line (Fig.4.4(a)), as in the case of ZGNR with 8-55 defects.

It is interesting to compare the cases of the 8-55 defect line in the armchair-CNT and the ZGNR under periodic boundary conditions. We show the tight-binding band structure of this latter case in Fig. B.2 of Appendix B. The defect-line bands behave similarly, and the differences

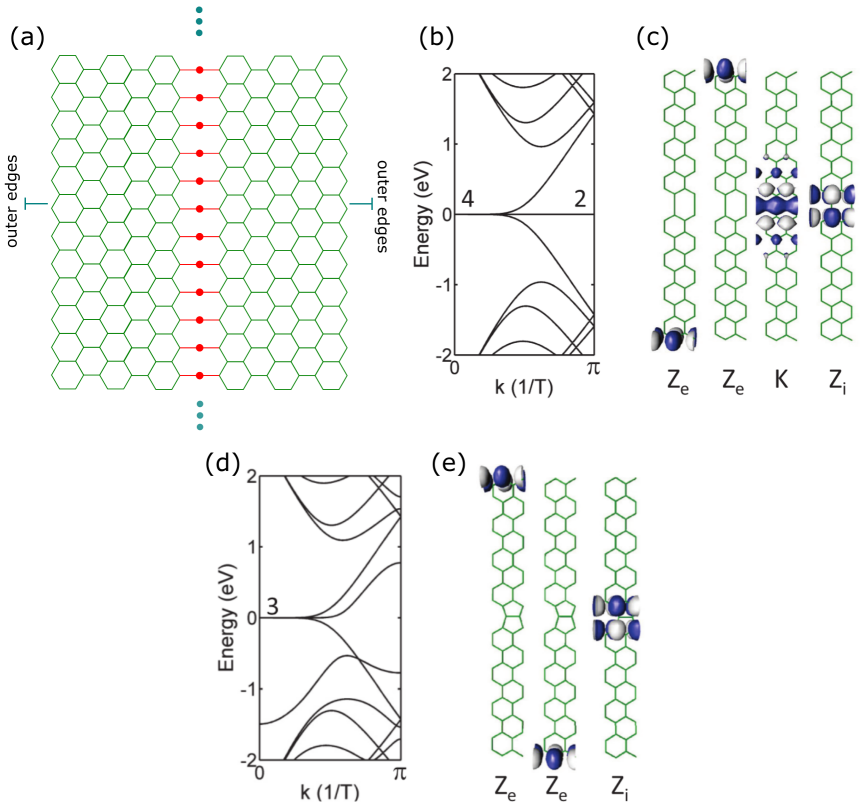

Figure 4.3: (a) Octagonal grain boundary in a ZGNR ribbon. Represented by red color are the Klein nodes which connect the two nanoribbon regions. (b) Electronic band structure using tight-binding calculation for two 8-ZGNR domains joined by the extra row of Klein-like atoms as in (a). The wavevector k is given in units of 1/T, where T is the length of the double unit cell along the grain boundary direction. The degeneracy in E = 0 bands at $k = 0$ and $k = \pi$ are indicated in the figure. (c) Tight-binding wavefunctions corresponding to the four zero-energy bands of (b) at $k = 0$. Blue and white colors denote positive and negative signs of the wavefunction, respectively. (d) Electronic structure of the ZGNR with a reconstructed 8-55 defect line calculated with tight-binding. (e) Wave-functions at k = 0 for the triple degenerated zero-energy bands of (d) at the Γ point. Taken from Ref. [106].

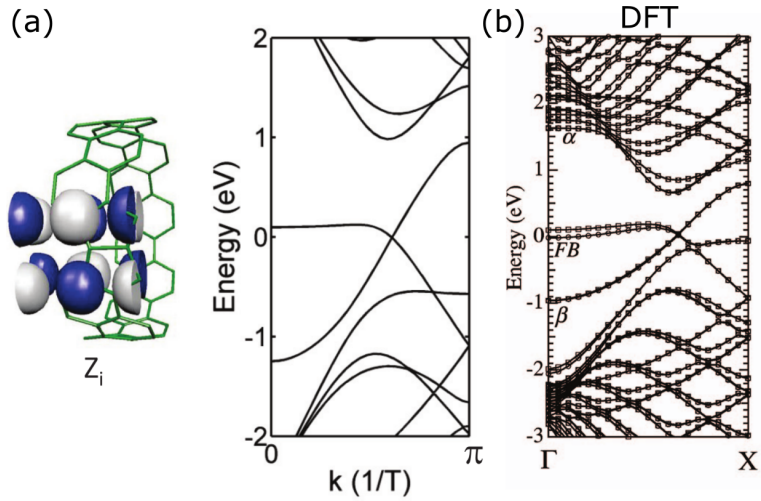

Figure 4.4: (a) Tight-binding wavefunction (left) at k = 0 for the band near the Fermi level and band structure (right) of an (8,8) armchair nanotube (rolling-up ZGNR) with a pentagons-octagons defect line. Taken from Ref. [106]. (b) Density functional theory band structure of the (10,10) nanotube with the pentagon-octagon defect-line using LDA and including spin. Squares and circles denote the energy band for the minority (β) and majority (α) spins, respectively. The DFT band structure figure is taken from Ref. [108].

rely on the number of unit cells used along the armchair directions. In our calculation, we use 20 rectangular graphene cells more than in the CNT model, so that the gap at the K point is reduced.

Density functional theory calculations have been performed on the array of 8-55 defected ZGNR [46]. The defect bands gain curvature along the ΓK path so thus that the electron-electron interactions play an important role in these systems. Similar results in CNT with an 8-55 defect line have been reported by Okada et al. [108] performing DFT calculation with spin-LDA functional, see Fig. 4.4(b). The bulk bands have a parabolic behavior and open a gap of ~ 1.0 eV at the K point. The defect states gain dispersion along the ΓK path near the Fermi level showing ferromagnetic coupling, which disappears near the K point. Thus, the 8-55 defect line hosts already interesting physics in single layer graphene systems, which deserves to be investigated with a larger number of layers. When a domain wall is included in gated bilayer graphene, topologically protected states appear in the gap around the K point (as detailed below), and are in the same region in which the 8-55 defect and bulk states mix each other in monolayer graphene. In this context, the topological and defect states can hybridize to create new physics in bilayer graphene systems.

Topological States in Gated Bilayer Graphene

We here review how gated bilayer graphene shows topological protected states when having AB-BA stacking changes. A graphene sheet is a bipartite lattice separated by **A** and **B** sublattices. These sublattices in bilayer graphene determine the stacking order between layers, the so-called AB stacking. The bilayer graphene band structure is gapless; nevertheless, applying a gate voltage induces a layer imbalance that causes a gap opening. Stacking domain walls can be created in BLG when separating AB from BA domains (Fig. 4.5(a)). For gated bilayer graphene the stacking change causes topologically protected states to appear in the gap [110]. In Figure 4.5(b), we display a scheme of the gated bilayer graphene band structure with a stacking domain wall.

The topological states are located at the K, K′ valleys and connect valence and conducting regions in pairs. The studies on gated BLG with a different kind of domain walls, such as strains and layer stacking walls, show this pair of topological states in the BLG bulk gap [111, 98]. Ex-

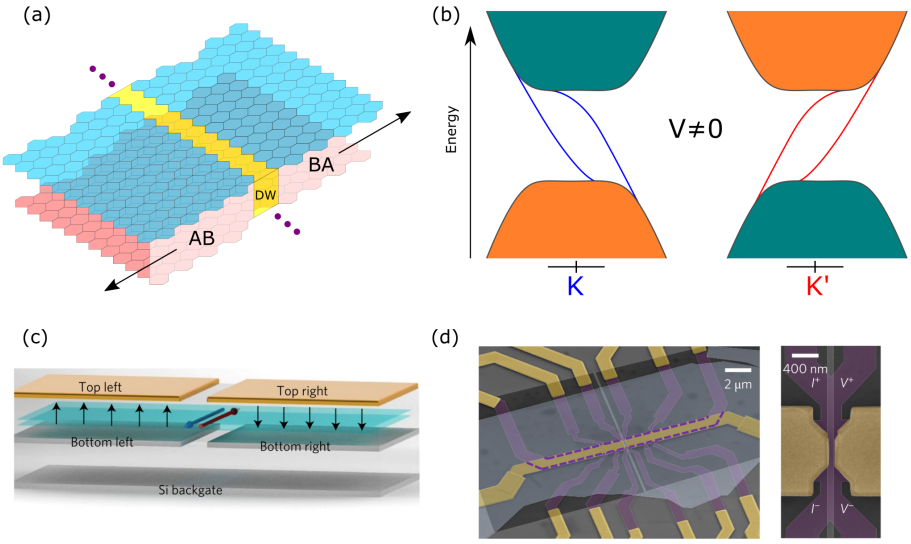

Figure 4.5: (a) Stacking domain-wall in bilayer graphene stacking. (b) Schematic band structure of gated bilayer graphene with a stacking domain wall considering no periodic boundary condition along the defect line. Topologically protected gapless states in blue (red) connect valence and conduction bands in K (K′) valleys. (c) Illustration of valley polarized electrical current in BLG domain wall. Blue and red states propagate in opposite directions addressed by the chirality of the K and K′ valleys. (d) SEM representation of an array of gate-voltage device where BLG region is shown in purple and gates in gold color. Taken from Ref. [109].

perimental studies on BLG have reported the presence of stacking domain walls [112]. These measurements show one-dimensional conducting channels corresponding to topological states along its edges. The conducting electrons propagate with opposite velocities in different valleys. In this sense, the valley chirality determines the electron propagation. Similar topological states can be shown in other ways to get stacking changes such as electric-field walls [113, 98]. Experiments also report on electric-field walls as shown in Fig. 4.5(c)(d) [109, 114]. Nevertheless, these systems prove to be challenging to be processed [109].

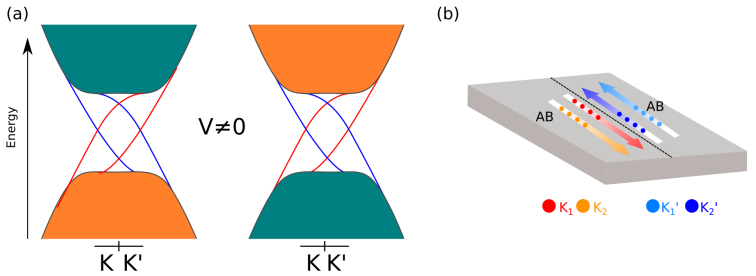

Figure 4.6: (a) Electronic structure of topological states on an array of domain walls in BLG. (b) Momentum propagation for topological states in (a) along the domain wall edge. Modified from Ref. [111].

Arrays of domain walls can be studied including periodic boundary conditions along *xy* directions. The array causes the appearance of an extra pair of topological states on each K and K′ valley [111]. In this context, two counter propagating pairs of topological states locate on each valley, as shown in Fig. 4.6(a). Thus the domain wall edge has two topological states per spin for each K, K′ point, see Fig. 4.6(b).

Non-trivial topologically protected states survive when a single 8-55 grain boundary is embedded in BLG (Fig. 4.7(a)) [115]. Its electronic structure using tight-binding calculation is shown in Fig. 4.7(b). [1] Because there is a 8-55 defect line between leads, the electronic structure shows a nearly negligible gap in the bilayer bands (Fig. 4.7(b)) as expected. The zero-energy band related to the defect line D disperses at

[1]The hopping factors used are $\gamma_0 = -2.66$ eV for the interatomic and $\gamma_1 = 0.1\gamma_0$ for interlayer.

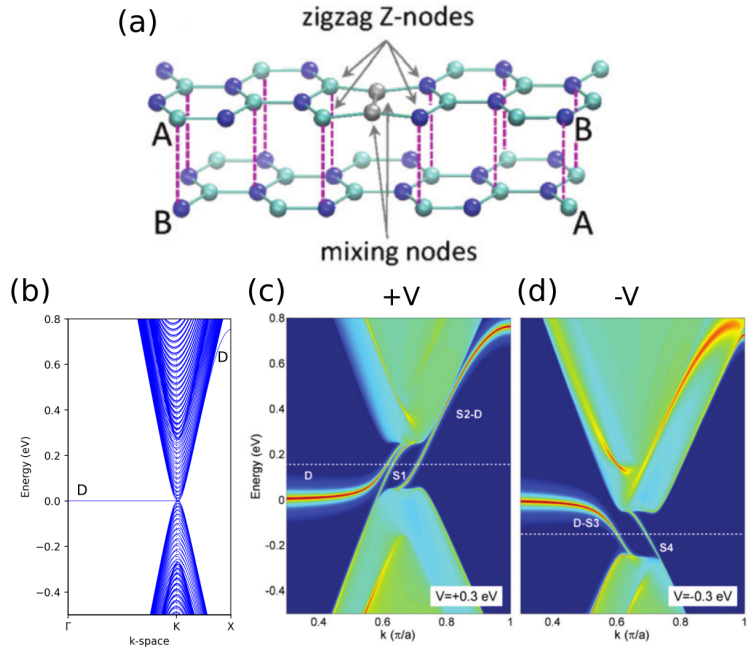

Figure 4.7: (a) Scheme of a defect-line in bilayer graphene. Cyan and blue colors show A and B sublattices, respectively. The Klein nodes, shown in gray color, mix the A and B sublattices. Defect-line nodes are shown with arrows; the zigzag nodes (Z) are in the top part. (b) Electronic band structure of a quasi-infinite BLG with a single 8-55 domain wall. (c), (d) Defect line region resolved local density-of-states LDOS(E,k) for the BLG with a 8-55 domain wall under positive and negative voltages. Panels (a), (c) and (d) from Ref [115].

the K point. Applying a gate voltage perpendicular to the surface makes that the bilayer graphene bands open a gap having topologically protected states. For positive gate voltages (Fig. 4.7(c)), the bands shift up in energy, and two topological states connect the valence and conduction regions that hybridize and mix with the defect band. For negative voltages (Fig. 4.7(d)), the bulk bands shift down in energies. However, contrary to the previous case, the gap hosts two bands connecting conduction and valence regions, and the defect band hybridized with one of the topological bands (D-S_3). Thus, the total number of states in the gap depends on the gate voltage orientation. Furthermore, the gapless states are layered resolved depending on the gate voltage polarization [115]. In summary, this study shows that topological and defect states hybridize, and the number of gapless states depends on the voltage polarization. How such hybridization occurs is the key to understand the physics behind the BLG with a 8-55 defect line. Because the usual tight-binding method ignores interactions between electrons, detailed calculations are required including these interactions. The electron-electron interactions would add different effects such as band dispersion and magnetism phases due to the defect line [105].

Based in the articles reviewed, we study an array of 8-55 defect lines to create a pattern of AB and BA domains. By including periodic boundary conditions along xy directions, we create an array of defect lines. We study the electronic properties of defect-line array using simple model, tight-binding, and density functional theory calculations including spin polarization. The simple model and tight-binding results let us to understand how the defect-line array and topological states are hybridizing. Density functional theory allows us to determine the effect of electron-electron interactions. Here we find that the defect-line states have ferromagnetic behavior in which spin-momentum locking occurs. To study the potential defect-line applicability on electronic devices, we perform further calculations involving not only external electric fields but also n-doping.

4.2 Structure and Basic Theory Models

Geometry of the system. The structure of an array of defect lines in Bernal stacked bilayer graphene is presented in Fig. 4.8(a). The supercell includes two stacking domain walls due to two topological defect lines in

each layer, which alternate an octagon and a pair of pentagons to form the grain boundaries between the AB and BA stacked regions of bilayer graphene. The supercell is composed of $L = 24$ primitive cells of an armchair nanoribbon in the x-direction. The defect line can be seen as joining two graphene edges, a pristine zigzag with a Klein-terminated edge [116]. For that reason, the defect nodes are labeled as zigzag and Klein, as shown in Fig. 4.8(c). In practice, every second pair of Klein nodes are dimerized and linked together, as observed experimentally [46].

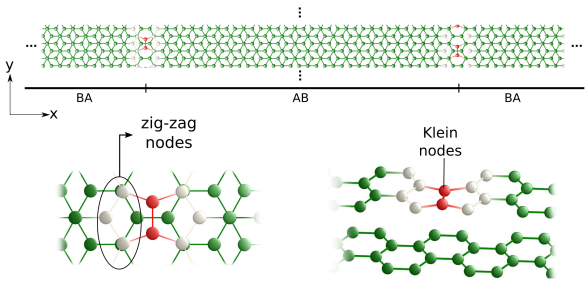

Figure 4.8: Unitcell of an array of defect lines in bilayer graphene that separate AB and BA domains. The region around defects is zoomed in the lower panels. The defect lines are separated by 12 primitive graphene unit cells, i.e. 5.24 nm.

Basic ingredients in a simple model. We first develop a simple model to understand how hybridization between the defect and topological states occurs. The effective model Hamiltonian that describes the interplay between gapless and defect states is written as follows,

$$\mathcal{H}(k) = \begin{bmatrix} k+V & 0 & \gamma_1 & 0 & 0 & 0 \\ 0 & -k+V & 0 & -\gamma_1 & \gamma_2 & 0 \\ \gamma_1 & 0 & k & 0 & 0 & \gamma_2 \\ 0 & -\gamma_1 & 0 & -k & 0 & 0 \\ 0 & \gamma_2 & 0 & 0 & H(k)k & 0 \\ 0 & 0 & \gamma_2 & 0 & 0 & H(k)k \end{bmatrix}, \tag{4.1}$$

where k corresponds to the y direction in reciprocal space. The upper 4×4 box is the two-layer graphene Hamiltonian for the topological states, and the lower 2×2 box includes the defect line states. Following reference

[117], the bilayer graphene Hamiltonian can be described by two graphene Dirac cones in each layer given as the diagonal $\pm k$ states, which interact through the coupling γ_1 between the layers; V is the gate voltage between the layers. As the hopping γ_1 does not mix states with $+k$ and $-k$, the gate voltage V does not open a gap, where the gapless topological states are remaining. We obtain that for bilayer graphene the Hamiltonian in Eq. 4.1 is taken with a small non-zero γ_1 value, set to 0.01 γ_0 (γ_0=-2.66 eV) to describe the interaction between layers. The defect states are included in the lower 2×2 box as two diagonal terms $H(k)k$, where $H(k)$ is the Heaviside function that includes dispersion when reaching the K, K′ valleys; they mix with opposite momentum and valleys in each layer. The coupling γ_2 in the Hamiltonian describes the interaction of the defect-line states with the $\pm k$ states ones.

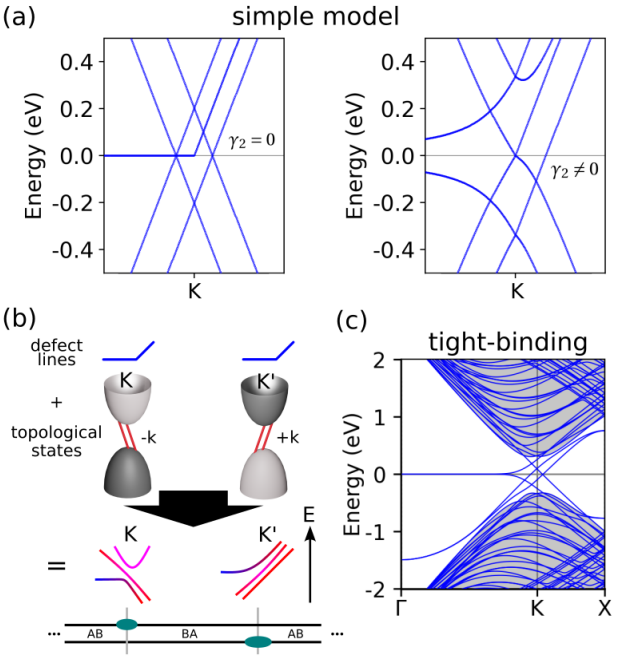

Figure 4.9: (a) Simple model bands for zero and non-zero γ_2 value. (b) Scheme of hybridization between gapless states in both valleys. (c) Tight-binding band structure of the array of defect lines shown in Fig. 4.8.

The left panel of Fig. 4.9(a) shows the electronic dispersion obtained from the Hamiltonian in Eq. 4.1 for $\gamma_2 = 0$ eV. The interlayer coupling (γ_1) leads to the topological gapless states behavior characteristic of systems where the bilayer stacking changes from AB to BA [41, 110]. These states connect the valence and conduction bulk bands with two pairs of bands with opposite velocities, each associated with one of the K, K′ valleys. We note that both Dirac cones split in energy showing the topological states in the middle.

For the non-zero γ_2 ($\simeq 0.10\gamma_0$), we obtain the electronic dispersion that is shown in the right panel of Fig. 4.9(a). Two of the topological states with $+k$ mentioned above remain even after coupling to the defect. The defect states split symmetrically away from the Fermi level and get opposite dispersions because they couple to topological states with different k velocities. The different behavior of the defect bands is due to the stacking change associated with the two opposite valleys, which correspond locally to each stacking change, i.e., each stacking change in bilayer graphene is a mirror reflection of the other by changing its relative chirality, as shown schematically in Fig. 4.9(b). Therefore, because the defect lines are located in different layers, their bands mix with opposite valleys having the two K and K′ values, which have opposite momenta due to the reflection symmetry.

Band structure within tight-binding approximation. In Figure 4.9(c) we display the tight-binding electronic dispersion for the structure given in Fig. 4.8 using the hopping value between the nearest carbon atoms. The bulk bands at the K point shown in grey have a gap due to the periodical stacking change induced by the defect lines. The width of the gap depends on domain size. In fact, the bulk band splitting is present when the system has gapless domain walls that also change locally the stacking between layers [110]. Within the gap, there are flat localized bands at the Fermi level along the Γ - K path. Specifically, the states at the Γ point are located at the defect line, and when they approach the K valley the bands become dispersive spreading from the defect states. In more detail, the dispersion near the Fermi energy is a result of the hybridization with the topological states, as already commented above.

4.3 Results and Discussion

4.3.1 Momentum-Locked Spin-Crossing

In this section, we present the results of DFT simulations performed for the array shown in Fig. 4.8 using the SIESTA package [118] and including a Van der Waals functional VdW-DF2 [54, 119]. We use a mesh cut-off of 600 Ry for the 3D grid of density and exchange-correlation potentials. We perform simulations relaxing the input structures in two dimensions and calculate their electronic properties. To adequately describe the electron distribution near the Fermi level, especially at the Γ point, the electron smearing is chosen to be small, about 0.1 meV. The corresponding converged mesh grid in the reciprocal space is thus large with 101×15 k-points grid for relaxed geometries. The relaxed geometry has in-plane carbon-carbon distances of about 1.44 Å and slightly different distances near the defect line. The most deformed hexagons are those that share edges with octagons and pentagons with lengths of 1.48 and 1.41 Å respectively. The detailed structure with the corresponding C-C distances is included in Appendix B.

We first analyze the band structure and then comment on the localization of defect states. Figure 4.10 shows the band structure of the array. Note that the array of defect lines induces a gap between the bilayer bands even though the system is not externally gated. The gap opening is typical of superlattices due to the finite-size effects. Furthermore, the array patterning reduces the periodicity of the bands dividing them into a series of subbands in the upper and lower bilayer valleys shown in the grey area.

Within the gap around K, we observe several gapless states. There are four intersecting bands that are divided into two pairs, and each of the pairs is related to one of the stacking changes. These four bands originate from the topologically protected states arising of defectless stacking domain walls [97]. Away from K, however, they hybridize with the localized states due to defect lines. This hybridization depends on the exact localization of the two types of states, namely, they interact if they are located in the same layer and sublattice [115].

There are states mostly localized on the defect lines. They are spin degenerate except for the two bands near the Fermi level, spanning from Γ to K. These two bands are nearly flat and their dispersion is related

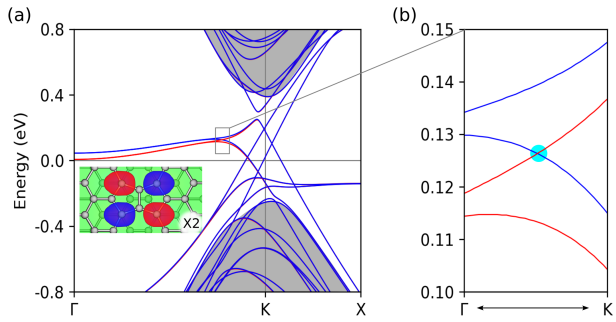

Figure 4.10: (color online) (a) Band structure of the array of defect lines. The gray-shaded regions are the bilayer bulk bands, showing a gap due to quantum size effects. The nearly flat states at the Fermi level are spin-split. The inset displays the wavefunction at the Γ point for an upper band state, which is localized at a defect line in the upper layer and degenerated with another similar state localized at the neighbor defect line in the bottom layer. Note that in the zoomed-in plot of the right panel (b), there is a spin crossing point near the K valley, marked by a cyan dot.

to electron-electron interaction: the bands are flat and partially occupied in calculations within the tight-binding approximation (compare with Fig. 4.9). There is a defect band associated with each of the defect lines in both layers. An example of the wavefunctions at the Γ point of the upper layer is shown in the inset of Fig. 4.10(a). We refer to them as defect bands due to the strong localization of those bands at zigzag nodes on both sides of a defect, being in this respect different from the edge states of terminated zigzag nanoribbons that are only localized on one edge [103, 106]. These defect bands hybridize with a pair of topological states related to the stacking change near the valleys.

The hybridized defect and stacking-change topological states show a spin-crossing point, marked in Fig. 4.10(b) with a cyan dot. The carrier momenta related to these two bands have opposite signs, which implies spin-momentum locking. Importantly, the wavefunctions of the two crossing bands are localized in different layers. Thus, currents related to spin-up and spin-down channels flow in opposite directions and are also spatially separated. The layer-resolved spin transport makes this array a possible candidate for engineering based on the spatial separation of the

spin currents [2].

4.3.2 Parallel Spin Couplings of Defect Lines under Gates

In the above simulations, the coupling spin configuration between lines is taken as ferromagnetic (FM) because it has the lowest energy. We now consider antiferromagnetic spin couplings (AFM) calculations and compare both results in Fig. 4.11. Then the initial spin configurations are set for the zigzag nodes as displayed in the schemes. The band structures of the FM and AFM phases are compared in the upper panels. They are almost the same except for the zigzag bands that are spin-degenerated in the AFM case, with spin polarization of opposite signs in each layer. We consider the effect of an external electric field E_{ext} on the two spin polarizations. We apply the field perpendicular to the surface with the values of 25.0, 50.0, and 107.5 mV/Å between the layers. Due to inversion symmetry, the same results are obtained for fields with opposite directions.

Figure 4.11(a) compares the evolution of the band structures of both magnetic phases under E_{ext}. While the bulk bands remain nearly spin degenerated, the effect of the electric field is clearly seen on the defect flat bands. In the FM case, it splits the two spin-down bands shifting down one of them in energy. The spin-up bands remain pinned at the Fermi level with a nearly constant value of spin polarization. The band splitting is also shown for the AFM coupling, that is degenerated for up and down polarizations. In the AFM case, a pair of spin-down bands split and one shift down in energy approaching the pair of pinned spin-up bands. The splittings increase and saturate for the value of $E_{ext} > 100$ mV/Å, for which the band structures for the FM and AFM couplings become similar. Although the order of the bands is different, the two middle bands are almost overlapping. In the FM coupling, they are localized at one defect, while the other pair of bands is located at the other one. The same pair of bands is located at the different defects in the AFM coupling. Thus, under an electric field the electronic behavior becomes the same, independently of the initial spin coupling. Furthermore, the magnetization for the FM case remains nearly constant with the field, while for the AFM case, it

[2] Although the crossing point is unoccupied, staying at $E \approx 0.1$ eV, negative doping is a way to reach the energy of the crossing bands, as discussed below.

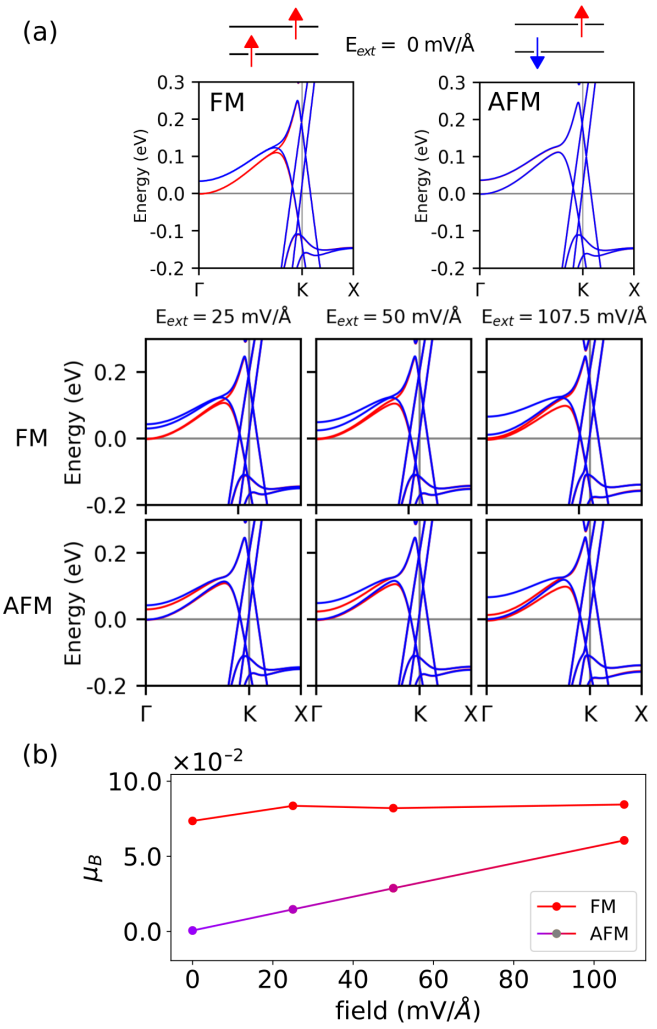

Figure 4.11: (a) Evolution of the band structure under electric field for the FM and AFM magnetic couplings between the defect lines. In both cases the bands seem saturated for a value of the field $E_{ext} > 100$ mV/Å. (b) Total magnetization versus field for the input FM and AFM couplings. The colors - red and blue - reflect the FM and AFM character, respectively. The line spins become ferromagnetically coupled with increasing.

increases towards the FM case, as shown in Fig. 4.11(b). It is worth to emphasize that using gates, the spins on defect lines in the array are easily aligned to be parallel between them.

4.3.3 Spin-Polarization of Valley States Induced by n-Doping

We next consider the influence of n-doping because we want to amplify and engineer the interesting electron-electron effects like spin polarization and magnetization. We look at the band structures of the array under different n-doping values from 0.3e to 1.3e. The bands are shown for some example values in Fig. 4.12. Previously studied degenerated bands, such as defect and bulk ones studied above, are now spin split, and the splitting is proportional to the doping value. The defect-located bands remain at the Fermi level, but the splitting between bands with the opposite spins increases; the spin-down bands shift up while the spin-up bands are bend down, becoming partially occupied at the Γ point. Because the BLG valley cone is shifted down in energy, the spin-crossing point between the defect bands becomes occupied for n-doping values larger than 0.6e, being here partially locked as one of the bands becomes nearly flat. We find that the valley bands shift down in energy while the defect bands stay pinned at their energies. The valley going down also induces that the corresponding topological and valley states become spin-polarized.

We study the impact of the electric field with n-doping structure. The band structures calculated when going from 0.3e to 1.30e are shown for two different n-doping values in Fig. 4.12 applying an electric field of 150.00 mV/Å, which is the regime of the band structure being almost saturated, i.e. when the gap width is large. Without doping, the defect bands are split with the middle pair of spin-up and spin-down being nearly degenerated. Under doping, the valley bands are shifted down in energy, but now the spin-degeneracy of all the bands have been lifted.

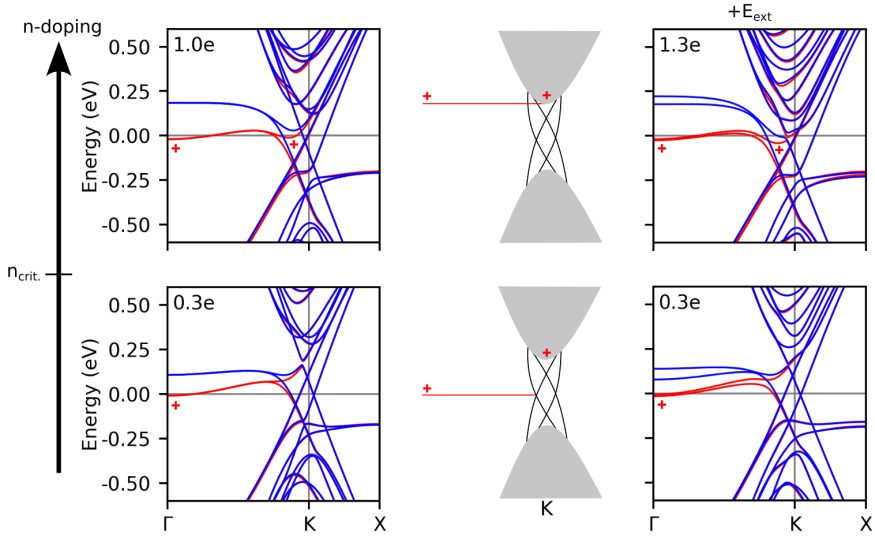

Figure 4.12: Band structure in the case of n-doping with values varying from 0.3e to 1.3e. Right panels correspond to have a field E_{ext} = 150 mV/Å. In the middle panels, we schematically illustrate that n-doping not only fills the defect bands, but also is pinning them. The topological and valley states are becoming occupied and spin-polarized.

Fermi Nesting and Charge Modulation

The n-doping causes not only the spin-up defect bands to shift down in energy and become occupied, but also the valley states to be partially occupied, as discused above. We next study the electron response function using the Lindhard theory. The band structure for an n-doping value of 1.0e is going through the high symmetry points in the whole 2D Brillouin zone in Fig. 4.13(a). We note that along the two-dimensional path the up bands are crossing the Fermi level several times. There are electron and hole pockets that suggest possible nesting on the Fermi surface. The spin-resolved density-of-states in the right panel indeed confirms that the spin-up bands are dominant around the Fermi level. The high density-of-states originates mainly from the two spin-up defect bands, here labeled A and B, which are intertwined with the valleys and topological states near the K point.

We then investigate the Fermi nestings by calculating the static response function. The unit cell of the superlattice has a large disproportion between the periodicity in the directions x and y. The 2D Fermi surface plot in the case of the B band is shown in inset of Fig. 4.13(b). They confirm the quasi-1D character showing nearly parallel lines along k_x that give rise to the maxima in the static response function. Figure 4.13(b) shows the response function $\chi(q_y)$ calculated for the spin-up bands A and B. It reveals strong peaks at $q_y^A = 0.29$ and $q_y^B = 0.32$ in $2\pi/a_y$ units for the A and B bands, respectively.

Large values of $\chi(q_y)$ suggest the possibility of charge density waves (CDW). We find especially interesting the case when the CDW is commensurate with the lattice, which means that the wavelength of the CDW is related to an integer number of repeating times the unit lattice constant. We establish that $\lambda_0^{CDW} = \frac{2\pi}{q_y} = \frac{N}{M} a_0$, where $\frac{N}{M}$ is a rational fraction, i.e., N and M can be found as integers. In that case, a Peierls instability takes place, and the distortions can induce further transitions from the ground state to a metastable state with lower periodicity [120]. The λ values corresponding to q_y^A is $\frac{N}{M} = 4.36$, which is a ratio far from being an integer. This wavelength can be ascribed to the defect line interacting with the topological states. This paves the way to understand the interaction of defects through topological states in general.

The q_y^B value, however, corresponds to an $\frac{N}{M} = 3.95 \approx 4$, being nearly

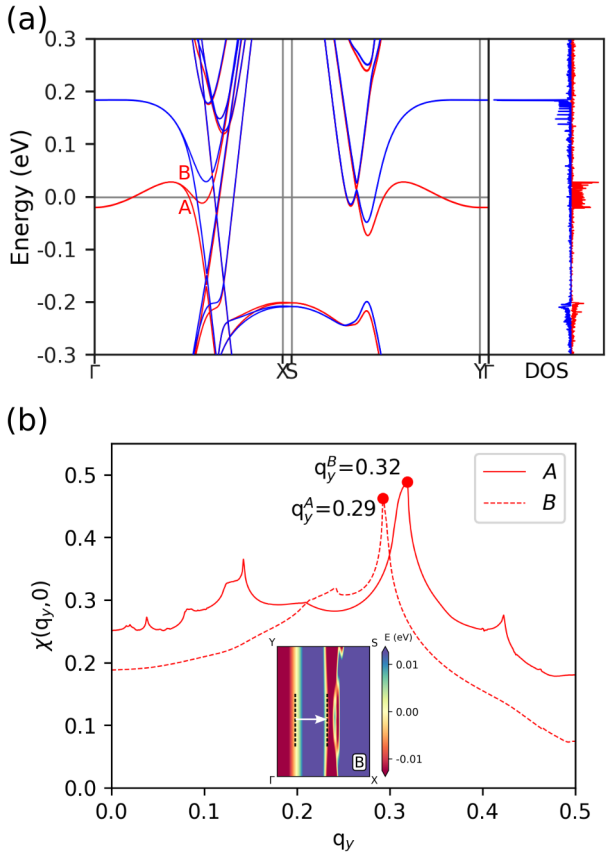

Figure 4.13: (a) Full band structure of the superlattice with n-doping along the two-dimensional Brillouin zone path. Red and blue colors correspond to spin-up and spin-down bands, respectively. The right panel shows the spin-resolved density-of-states. Note that the spin-up bands become crutial around the Fermi level. The labels A and B denotes the two spin-up bands near the Fermi energy. (b) Static response function of the A and B spin-up bands. The peak in the B band corresponds to commensurate charge density wave (see details in text).

integer. It is related with the electron-electron interaction between the defect line and the valley states. On the one hand, going beyond this theoretical results, it could result in a Peierls instability and form a ground state with a distorted lattice by allowing a lower periodicity in charge densities using larger supercells of the order of four times along the defect line which is beyond calculations in this study. On the other hand, possible experiments such as using scanning tunneling microscopy (STM) seems a common way to study the appearance of charge densities oscillations in carbon nanostructures along line defects, similar to our results for quantum dots of carbon nanotubes [121]. [3]

4.4 Conclusions

In this study we investigate an array of defect lines in bilayer graphene that introduce stacking change, creating a superlattice of alternate AB and BA stacking domains. In the electronic structure we observe the interplay between bands which are related to topological and defect line states. We focus on defect bands that show spin-momentum locking under a ferromagnetic phase between the defect lines. Under electric field, the magnetic moment in the antiferromagnetic coupling also tends to be as in the ferromagnetic case. We next apply n-doping to the array. The bulk bands shift down in energy, and the spin-up defect bands become partially occupied so that the defect bands get pinned at the Fermi level. Furthermore, the pinned bands are nested under n-doping. We find that they correspond to a commensurate charge-density-wave which could be related to Peierls instabilities. The spin momentum locking states are filled for n-doping values larger than 1.0e. When we combine doping and large values of field, the electronic structure is dominated by the n-doping, but the defect bands split as in the field case. The array of defect lines can play a role as one-dimensional conducting channels. Because arrays of stacking grain boundaries such as 8-55 defect line are drawing much attention of the experimental community [122], we are looking forward to measurements that confirm the electronic phenomena predicted in this

[3] In fact, the two wavelengths could show an interference pattern with beatings that could translate into commensurate and incommensurate regions being measured along the line defects.

work.

5 — General Conclusions and Outlook

In this thesis we use density functional theory to study few-layered graphene systems. We note that the stacking between graphene sheets plays an important role when looking at its electronic properties and therefore in the design of electronic devices. We determine which deformations destabilize the rhombohedral stacking in trilayer graphene against the Bernal one. In addition, we examine an array of 8-55 defect lines that induces periodic stacking changes in bilayer graphene; its electronic structure shows a mixing between topological and defect states.

Firstly, we note in chapter 3 that rhombohedral trilayer graphene is more stable than its Bernal counterpart. We perform structural deformations of both stackings to determine the ones that induce the Bernal order being more stable than the rhombohedral one. We have seen that the Bernal stacking is more stable by a few meV/nm^2 when doing in-plane stretching. Out-of-plane deformations induce that the Bernal stacking is more stable when decreasing interlayer distances. We perform shear deformations and analyze the relative energy; we notice that the relative energy difference goes up to tenths of meV/nm^2. The rhombohedral stacking is more stable for values of $\phi < 30°$, and for larger values the Bernal stacking shows lower energies with 60° periodicity. In addition, we perform calculations with sublattice displacements that break the symmetry between layers. We find that the stability of the two trilayer stackings is exchanged depending on which sublattice is shifted. The sublattice displacement can occur when contaminants appear between trilayer graphene layers. In general, we believe that these deformations occur during experimental steps such as heating, cooling cycles to pattern contacts on few-layer graphene

samples.

In chapter 4 we investigate an array of 8-55 defect lines in bilayer graphene. Using tight-binding calculations, we find that periodic stacking change induces a gap in the bulk bands. The gap reveals topological states typical of bilayer graphene under periodic stacking changes. Furthermore, the 8-55 defect lines provide flat bands at zero energy, which are strongly localized on the edges of the defects. The defect states locate on each layer and hybridize with topological states related to different valleys of the Bernal stacking.

Next, we perform DFT calculations to consider electron-electron interactions for the array. The defect bands gain dispersion and are spin polarized. They show spin-momentum locking for the ferromagnetic phase between moments induced by defect lines. We then compare ferromagnetic and antiferromagnetic spin polarizations under several values of the electric field. When we increase the electric field, the band structure in the FM and AFM phases shows nearly similar behavior. In fact, the magnetic moment in the AFM phase becomes as in the FM case. Further, we include n-doping in the array of defect line because the bulk bands shift down in energy and spin polarization would increase. Indeed, the defect bands get partially occupied, pinned to the Fermi level, and increase their spin polarization. The shifting of the bulk bands and the pinning of the defect ones cause that the states involved in the spin-momentum locking are occupied for the n-doping values larger than 1.0e. The field in addition to n-doping induces spin splitting of the defect bands with the same spin polarization. With n-doping, the spin-up defect bands pinned around the Fermi level can also be nested. We study this nesting and find commensurable charge density waves, which could be related to Peierls instabilities. This result asks for experimental confirmation like STM measurement which already is a common procedure to observe charge modulations in carbon nanostructures. The array of defect lines can be interpreted as one-dimensional conducting channels that preserve its spin polarization even in the presence of an electric field and n-doping. Furthermore, because the 8-55 grain boundaries have been observed in graphene [46], we are looking forward to experimental measurements that confirm our results considering arrays of stacking domain walls [122].

Outlook. In summary, the studies of this thesis show that stacking plays an essential role in the electronic properties of graphene-like systems. We note that graphene stacking is crucial in the design of electronic devices to accomplish specific tasks. Because these devices are getting smaller and smaller - and thus their areas - the stacking can be engineered. We expect that the deformations studied in this thesis could help to develop strategies to avoid stacking changes of the interesting rhombohedral phase. It is usual in few-layer graphene samples to find grain boundaries that cause the stacking change. The electronic properties predicted, such as spin-momentum locking and charge density waves, should be checked with experimental observations to ensure that they are sufficiently robust in real systems.

Appendices

A — On the Relative Stability Between Trilayer Graphene Stackings

A.1 Convergence Tests

In Chapter 3, we examine the relative stability between Bernal and rhombohedral stacking. The energy differences between both stacking orders are below meV/nm^2 which are in the same order of van der Waals (vdW) interactions. The vdW interaction in an experimental sample depends on the surface area; in this context, experimental samples are going to be stabilized when they reach a critical area, so that their layers are locked in a stacking order and sliding is avoided. Otherwise, the layers would be switching between different stackings at room temperature. We need to assess convergence tests in more detail than for other materials. These tests look at cut-offs, broadening energies values and k-meshes. Our strict energy difference criterion goes down to 10^{-3} meV per nm^2, and the self-consistent electronic energy tolerance should be well below this threshold. The energy for each stacking in our calculations should be stable. We then choose the electronic self-consistency tolerance about 10^{-8} eV. We use the forces criterion of μeV/Å for geometry relaxations. These two criteria causes that the stacking energy differences are in the order of tenths or hundreds of meVs.

Cut-off Energy Test

We present an energy cut-off convergence test for the plane-waves basis set. We firstly use a k-mesh of 30×30×1 k-points. The electronic smearing broadening value is $\sigma = 0.05$ eV. Figure A.1 displays the Bernal and rhombohedral stacking energy difference versus cut-off. The blue line marks the cut-off value of 700 eV considered in our study. The energy difference value obtained for this test is within our criterion (μeV per nm^2) much below the value of the energy differences discussed in Chapter 3.

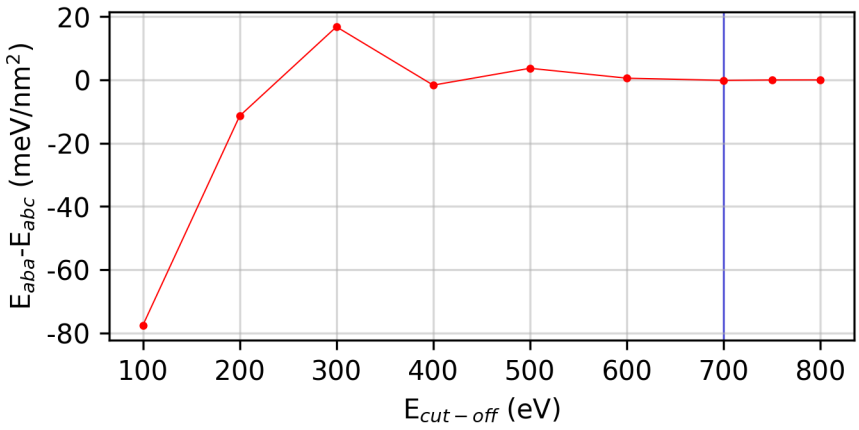

Figure A.1: Convergence test for energy differences between the Bernal and rhombohedral stacking against kinetic cut-off energies.

Broadening Energy Test

Next test is to converge the broadening value σ in the discrete integration points of the Brillouin zone. The broadening is crucial, especially to describe the electronic band states near the Fermi level and, thus, the occupation of ground states. When the σ value is too large in the smearing function, some conduction band states are fully or partially occupied. When having large σ values, the split states near the Fermi level can be also overlooked by averaging. When the σ value is too small the energy levels behave like as being a discrete set. In order to optimize the smearing

value, we consider a gaussian smearing using an energy cut-off of 700 eV and a k-mesh of 30×30×1. Figure A.2 shows the stacking energy difference as a function of the σ values. We mark the selected sigma value to be used in the following with a blue line at 10^{-2} eV, which shows the minimum stacking energy difference. This energy difference is 9.87 meV/nm^2. It is also noteworthy that the chosen σ value can discriminate the splitting between the flat valence and conduction bands around the K and K' points for rhombohedral stacking.

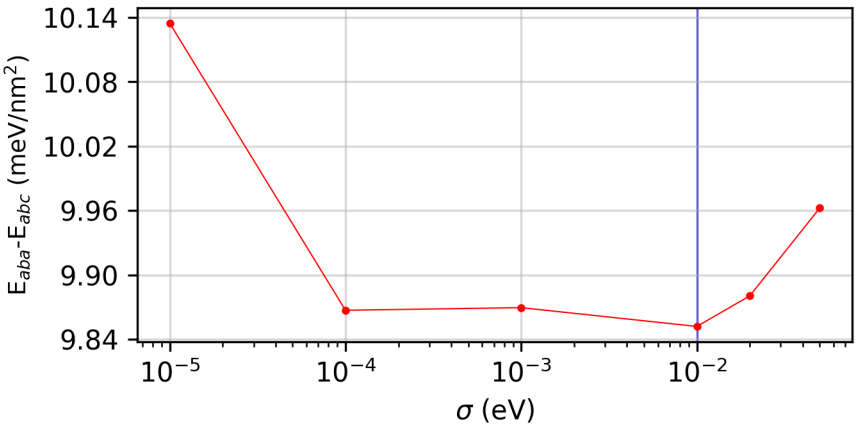

Figure A.2: Convergence test for the stacking energy difference against the broadening energy (σ) using gaussian smearing.

K-mesh Energy Test

The relevant physics of trilayer graphene occurs mainly around the low-energy bands. We focus our attention on the K and K$'$ points because the states around that points are behind the stacking order stability. The anisotropic deformations of the hexagonal lattices in graphene systems induce displacement of high-symmetry points on its irreducible Brillouin zone; specifically, the K and K$'$ points are not included when using a 30×30×1 k-mesh grid. Therefore, we perform the k-mesh energy tests taking into account the relative energy difference detailed in the main text. We generate a regular Monkhorst-pack grid centered at the Γ point as

required by hexagonal lattices. Figure A.3 presents the energy difference between the ABA and ABC stackings versus the number of k-points in the k×k mesh. We note a pattern not so common during the k-test. The red curve corresponds to energy differences for $k_x \times k_y \times k_z$ meshes with the k_x and k_y numbers being a multiple of 3, while the broad gray curve collects the points obtained with other k-meshes. Both curves show qualitative differences: the gray points show negative energies for k-mesh values below 100×100×1, implying that Bernal stacking is more stable than the rhombohedral one. Note that these energy differences show a non-monotonous trend when compared to the red curve. Contrary to these results, the red curve following the multiples of 3 k-meshes shows stability for the rhombohedral case. For our energy tolerance criteria (10^{-3} meV/nm2) the energy differences are stabilized for k-meshes larger than 174×174×1. As pointed out before, the K and K′ points in graphene contain the relevant physics under the Fermi energy; therefore, omitting these points could also yield incorrect qualitative energy trends when calculating the relative energy difference.

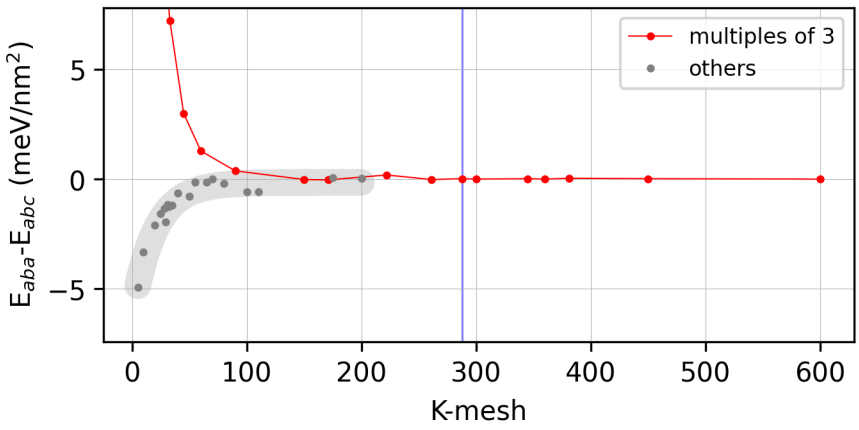

Figure A.3: Differences in stacking energies versus the number of k-points in the reciprocal mesh. The red curve corresponds to a reciprocal-mesh grid being $k_x \times k_y \times 1$ with the k values multiple of 3 in the plane and including the K and K′ points; the thick gray curve collects all other cases. For the k-values larger than 174, the energy differences are converged to the required accuracy limit.

When we investigate the anisotropic lattice deformations, regular Brillouin zone samplings may not include the high symmetry graphene points. Thus, a very fine k point sampling is required unless the k-points are commensurate with the two orthogonal directions in the plane. Our k-mesh is taken as 288×288×1, marked in blue in Fig. A.3, which produces well-converged energies even for the anisotropic deformed lattices. Here, the relative energy difference is 0.60 meV/nm^2. Furthermore, we test the k-mesh sampling by adding or not by hand the missed high symmetry points and modifying the corresponding weights to show their relevance. The stacking energy differences of k-meshes larger than 174 agree using the two types of k-meshes within μeV per nm^2, indicating that the band structure for deformed layers is well described by the regular k-mesh sampling considered above.

A.2 Comparison of Different VdW Functionals

We study the stacking energy difference by using several density functionals for the van der Waals interaction between layers. We are using the following parameters: a cut-off energy of 700 eV, a smearing factor of 0.01 eV, an electronic self-consistent energy tolerance of 10^{-8} eV, a k-mesh of 30×30×1, and a force tolerance for the relaxations of atoms and cells of μeV/Å. Figure A.4 collects the energy differences between the Bernal and rhombohedral stacking. Here we use the most common functionals used for dispersive interactions. For all the tested functionals the energy differences between stacking orders is small - few meV/nm^2- and shows that the rhombohedral stacking is favorable against the Bernal one.

The local density approximation (LDA) gives us a good approach to the structural stability and the study of vibrations in multilayered graphene systems. The energy difference is 9.44 meV/nm^2 showing that the rhombohedral stacking has lower energy than the Bernal one. Nevertheless, because it is a local approximation, corrections to reproduce long-range interactions for sparse matter must be included in the form of non-local interactions.

Therefore, we use the Grimme correction which within a general gradient approximation (GGA) to the exchange-correlation energy term [123] is a semi-empirical adjustment to the non-local and long-range interactions.

We test two generally used Grimme flavors: the vdw-D2 and the damped one vdw-D3 [124, 125]. These functionals yield similar energy differences of 8.57 and 10.49 meV/nm2, respectively.

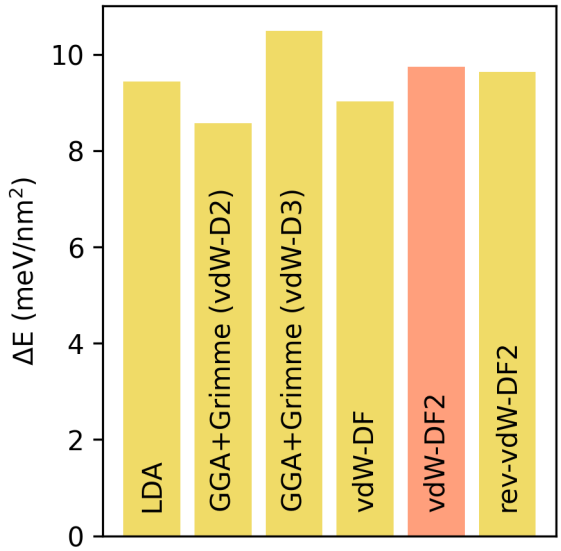

Figure A.4: Stacking energy differences ($\Delta E = E_{aba}$ - E_{abc}) using several functionals to deal with non-local disperse interactions.

Next, we study the vdw-DF functional, which is one of the latest functionals to study vdW-like systems [56]. The non-local exchange-correlation energy follows the expression $E_{xc}=E_x^{GGA} + E_c^{LDA} + E_c^{nl}$, where the subscript *nl* indicates the non-local contribution. Using this functional the rhombohedral stacking order is more stable with a relative energy of 9.02 meV/nm^2. Following the same family of functionals we test the vdw-DF2 one. This functional is designed to describe sparse systems in biological matter applications and organic elements involved in carbonaceous systems [54, 126, 80]. The vdw-DF2 functional improves the non-local correlation term. It replaces the revPBE exchange term in vdw-DF functional with a PW86 term [127], where the former is more repulsive [128]. The relative energy difference calculated by vdw-DF2 is 9.74 meV/nm^2, which is nearly the same result obtained before. Finally, we consider the rev-

vdw-DF2 functional, which is one of the modern versions of the vdw-DF family designed for inhomogeneous systems [55]. The energy difference is given as 9.64 meV/nm^2, which agrees with all previous calculated VdW functionals. We consider the vdw-DF2 functional to perform best for our calculations. This functional describes better the interlayer interaction of graphene, where functionals of this family seem to overestimate the interlayer distance and the binding energy [129].

A bibliographic search shows no clear agreement on which functional have to be considered, specially in systems like layered graphene because the performance each functional is still under discussion. We found that functionals correctly reproduce the interlayer distance, but they fail when estimating the binding energies including pure graphite. Although many functionals have shown acceptable performance in clusters and molecules, functional transferability is now under discussion. These discussions are important because few-layered-like systems show today emergent properties. For example, systems like TLG do not behave exactly like graphite concerning the interlayer distances and, more importantly, their electronic properties are different [129, 130, 131].

A.3 Limits of Shear Lattice Deformations

The simulations of the shear deformations on trilayer graphene structure were performed for different azimuthal (ϕ) and polar (θ) angles. We display the valid ϕ or θ angles values in Fig. A.5, when the Bernal and rhombohedral interlayer nearest neighbors are preserved. The gray data correspond to the ϕ and θ angles that cause a change in the interlayer nearest neighbors. Thus, we can no longer treat such structures as being purely Bernal or rhombohedral. The blue and red dots correspond when the Bernal and rhombohedral stacking nearest neighbors are preserved, respectively.

We note that the periodicity of the Bernal and rhombohedral stackings are different. The former have a periodicity of 60 degrees, while the latter have 120 degrees. Therefore, the relative stability between stackings follows the lower periodicity as shown in the inset panel of Fig. 3.9 described in Chap. 3.

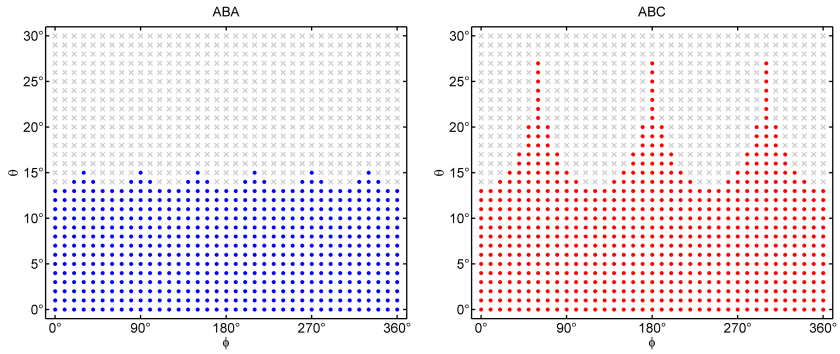

Figure A.5: Close stackings to the Bernal and rhombohedral geometry under shear deformation. Dots refer to the values of the θ and ϕ angles for which the stacking geometry is nearly preserved, crosses when we no longer can call these structures as being Bernal and rhombohedral.

Electronic Bands of Rhombohedral Trilayer Graphene under Shear

The shear on the Bernal and rhombohedral stackings modifies the interlayer coupling and changes thus their electronic structure. Here, we examine the changes in the electronic structure of the rhombohedral stacking because the changes in its low-energy bands seems relevant. This study is related to how shear deformations affect van Hove singularities near the Fermi energy. In figure A.6, we present the rhombohedral stacking band structure for a shear of $\theta = 5°$ and $\phi = 0°$. In grey, we display the case without shear showing almost electron-hole symmetry next to the Fermi level around the K and K$'$ points, those bands are labeled as primary bands, and the following bands around ± 0.25 eV are called as secondary bands. When analyzing the shear case, the electron-hole symmetry is lost. The bands move down in energy along the ΓK path, while those along KM path move to the left with a crossing of bands at the K point. The secondary bands come from interlayer nearest neighbors interaction [132]. The primary bands stem from uncoupled outer layer sublattices, also called hollow sites. These bands take part of the flat regions around the K and K' points and are related to the van Hove singularities near the Fermi energy. Under distortions, shear makes that the interlayer coupling

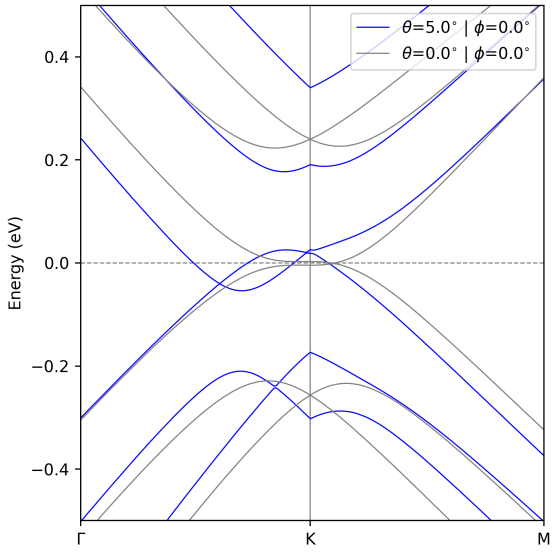

Figure A.6: Electronic band structure for pristine (gray) and shear rhombohedral (blue) trilayer graphene.

is enhanced by tilting. For $\theta > 0$, the shear causes a shifting between layers and tilting of the stacking layers. Consequently, we note redistribution in the band structure with respect to the undistorted case next to the Fermi level, and the van Hove singularities are expected to split. The charge redistribution comes from states located in hollow sites at the top and bottom layers. Then, the van Hove singularities are moved away from the Fermi level. Additionally, the charge redistribution matches with the band behavior along the KM path line. Here, the shift and translation in energy can be explained by the "trimerization" of carbon atoms between layers in a way that one-dimensional patterns are formed, an assumption which is reasonable regarding how shearing breaks the symmetry.

B — Details for the Calculations in the Defect Line Array

B.1 Structural Optimization

We perform a geometry relaxation to optimize the supercell presented in Sec. 4.2. Within density functional theory, we use SIESTA together with a vdw-DF2 functional to reproduce the non-local dispersion energies [54]. The relaxations considers the following list of parameters: an energy cut-off 600 Ry, a tolerance for ion forces of 1.9 meV/Å, a smearing of 10 meV, and a k-mesh of 31×31×1. The resulting interlayer distance is 3.66 Å, and the geometry relaxations slightly increase almost all the intralayer carbon-carbon bond lengths. We collect these lengths on the histogram of Fig. B.1. We note that the carbon-carbon distances are slightly larger than the pristine graphene one (1.42 Å, marked in dashed gray line) on average.

On the lower panel, we present the lattice structure around the defect-line with colors representing the bond lengths. The largest bond lengths are next to octagonal defects, and the smallest ones are in the pentagons. The bonds of the next layer below the defect-line are similar to the ones away from the defect line in the top layer.

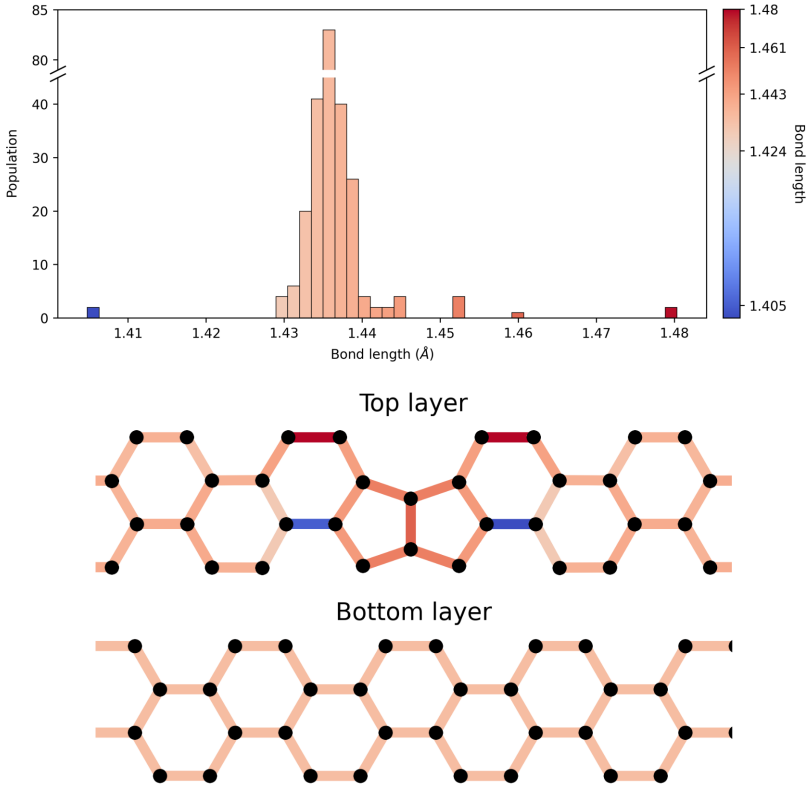

Figure B.1: Histogram of the bond lenght in the relaxed defect line array geometry. The relaxed structure around the defect-line is shown below; the colors correspond to the bond lengths following the color bar of the histogram.

B.2 Tight-Binding and non-polarizes DFT Electronic Structure

We study the origin and behavior of the bands by performing electronic structure calculations for monolayer and bilayer systems. We include calculations of a monolayer with a defect line for comparison purposes. We use atomistic calculations using tight-binding (TB) and non-polarized density functional theory (DFT). Regarding the TB method, we consider an intralayer hopping factor of $\gamma_0 = -2.66$ eV and an interlayer hopping factor of $\gamma_1 = 0.1\gamma_0$, following Ref. [115]. The hopping factors are taken up to the first intralayer and interlayer nearest neighbor. In addition, we use supercells to perform these TB and DFT calculations. We are dealing with an array of defect lines even in the monolayer case.

We present our results in Figure B.2. We note that the bulk bands with curvature at the K point split, creating a gap that reveals the defect states on each panel. These defect states have the same origin as discussed in Chapter 4, being related to zigzag nodes - at zero energy- and Klein nodes- in the energy range from -1.0 to -1.5 eV at the Γ point. Following the tight-binding calculations, the defect states cross below the Fermi level when approaching the K point in the monolayer case. Around the same point, we note the main differences with the bilayer case that shows four bands crossing at the gap.

We note a similar band behavior regarding the DFT calculations than in the TB predictions. In the monolayer case, the defect band around the Fermi level gets dispersed because electron-electron interactions are included in DFT. These interactions move the crossing bands around the K point above the Fermi level for the monolayer case.

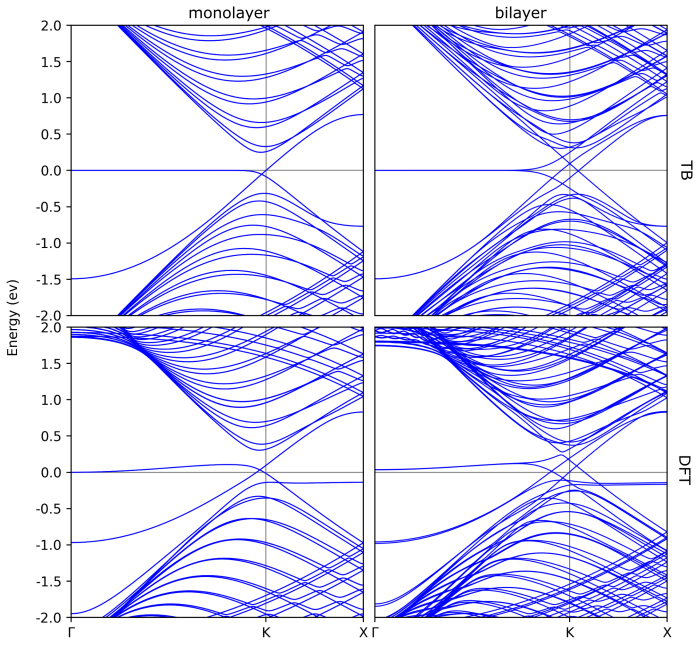

Figure B.2: Electronic structure of a array of defect lines with the length of $L = 24$. Comparison between monolayer and bilayer cases calculated with tight-binding and non-polarized density functional theory.

B.3 Fermi Surface Defect-line States

We calculate the Lindhard function using the Fermi surfaces obtained from DFT calculations. Here we focus on the A and B labeled zigzag spin-up band surfaces with n-doping (1.0e). A finest Brillouin sampling is required to assess the Fermi surface correctly. Therefore, we set a fine k-mesh of 101×15×1 using the Monkhorst-pack procedure [133]. Because the A and B bands are next to the Fermi level, we use a smaller smearing broadening factor equal to 0.1 meV for these studies.

Figure B.3 shows the energy colormap of the A and B bands in the rectangular Brillouin zone, where the lighter regions correspond to the Fermi surfaces showing a quasi-1D-like shape. From left to right, the edges of the Fermi surfaces connected by arrows are the ones which yield the largest contribution in the response function of the A and B bands.

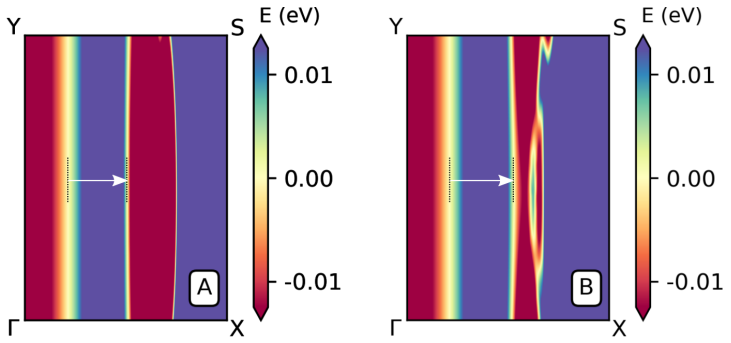

Figure B.3: Fermi surface in the whole rectangular Brillouin zone of the *A* and *B* defect bands shown in Fig. 4.13 of the main text.

Bibliography

[1] Changhao Liang, Kazuya Terabe, Tsuyoshi Hasegawa, and Masakazu Aono. Resistance switching of an individual ag_2/ag nanowire heterostructure. *Nanotechnology*, 18(48):485202, 2007.

[2] P. Drude. Zur elektronentheorie der metalle. *Annalen der Physik*, 306(3):566, 1900.

[3] P. Drude. Zur elektronentheorie der metalle; II. teil. galvanomagnetische und thermomagnetische effecte. *Annalen der Physik*, 308(11):369, 1900.

[4] E. Schrödinger. Quantisierung als eigenwertproblem. *Annalen der Physik*, 384(4):361, 1926.

[5] P. A. M Dirac. The quantum theory of the electron. *Proceedings of the Royal Society of London. Series A, Containing Papers of a Mathematical and Physical Character*, 117(778):610, 1928.

[6] Léon van Hove. Von neumann's contributions to quantum theory. *Bulletin of the American Mathematical Society*, 64(3):95, 1958.

[7] John Von Neumann. *Mathematical Foundations of Quantum Mechanics*. Princeton University Press, 1996.

[8] W. Heitler and F. London. Wechselwirkung neutraler atome und homöopolare bindung nach der quantenmechanik. *Zeitschrift fur Physik*, 44(6-7):455, 1927.

[9] P. Hohenberg and W. Kohn. Inhomogeneous electron gas. *Physical Review*, 136(3B):B864, 1964.

[10] W. Kohn and L. J. Sham. Self-consistent equations including exchange and correlation effects. *Physical Review*, 140(4A):A1133, 1965.

[11] Royal Swedish Academy of Sciences. The Nobel Prize in Chemistry 1998, 1998.

[12] John Desmond Bernal. The structure of graphite. *Proceedings of the Royal Society of London. Series A, Containing Papers of a Mathematical and Physical Character*, 106(740):749, 1924.

[13] M.S. Dresselhaus and G. Dresselhaus. Intercalation compounds of graphite. *Advances in Physics*, 30(2):139, 1981.

[14] T.A. Land, T. Michely, R.J. Behm, J.C. Hemminger, and G. Comsa. STM investigation of single layer graphite structures produced on pt(111) by hydrocarbon decomposition. *Surface Science*, 264(3):261, 1992.

[15] R. F. Frindt. Superconductivity in ultrathin nbse$_2$ layers. *Physical Review Letters*, 28:299, 1972.

[16] Y. Ohashi, T. Koizumi, T. Yoshikawa, T. Hironaka, and K. Shiiki. Size effect inthe in-plane electrical resistivity of very thin graphite crystals. *TANSO*, 1997(180):235, 1997.

[17] Royal Swedish Academy of Sciences. The Nobel Prize in Physics 2010, 2010.

[18] Alfonso Reina, Xiaoting Jia, John Ho, Daniel Nezich, Hyungbin Son, Vladimir Bulovic, Mildred S. Dresselhaus, and Jing Kong. Large area, few-layer graphene films on arbitrary substrates by chemical vapor deposition. *Nano Letters*, 9(1):30, 2009.

[19] Hoonseung Lee, Maria Antoaneta Bratescu, Tomonaga Ueno, and Nagahiro Saito. Solution plasma exfoliation of graphene flakes from graphite electrodes. *RSC Advances*, 4(93):51758, 2014.

[20] Buddhika Jayasena and Sathyan Subbiah. A novel mechanical cleavage method for synthesizing few-layer graphenes. *Nanoscale Research Letters*, 6(1):1, 2011.

[21] Royal Swedish Academy of Sciences. The Nobel Prize in Physics 2010, 2010.

[22] Jae Hun Seol, Insun Jo, Arden L. Moore, Lucas Lindsay, Zachary H. Aitken, Michael T. Pettes, Xuesong Li, Zhen Yao, Rui Huang, David Broido, Natalio Mingo, Rodney S. Ruoff, and Li Shi. Two-dimensional phonon transport in supported graphene. *Science*, 328(5975):213, 2010.

[23] Alexander A. Balandin, Suchismita Ghosh, Wenzhong Bao, Irene Calizo, Desalegne Teweldebrhan, Feng Miao, and Chun Ning Lau. Superior thermal conductivity of single-layer graphene. *Nano Letters*, 8(3):902, 2008.

[24] R. R. Nair, P. Blake, A. N. Grigorenko, K. S. Novoselov, T. J. Booth, T. Stauber, N. M. R. Peres, and A. K. Geim. Fine structure constant defines visual transparency of graphene. *Science*, 320(5881):1308, 2008.

[25] K. S. Novoselov. Nobel lecture: Graphene: Materials in the flatland. *Reviews of Modern Physics*, 83:837, 2011.

[26] J. Scott Bunch, Arend M. van der Zande, Scott S. Verbridge, Ian W. Frank, David M. Tanenbaum, Jeevak M. Parpia, Harold G. Craighead, and Paul L. McEuen. Electromechanical resonators from graphene sheets. *Science*, 315(5811):490, 2007.

[27] Nguyen Hong Shon and Tsuneya Ando. Quantum transport in two-dimensional graphite system. *Journal of the Physical Society of Japan*, 67(7):2421, 1998.

[28] J. W. McClure. Diamagnetism of graphite. *Physical Review*, 104:666, 1956.

[29] D. P. DiVincenzo and E. J. Mele. Self-consistent effective-mass theory for intralayer screening in graphite intercalation compounds. *Physical Review B*, 29:1685, 1984.

[30] Gordon W. Semenoff. Condensed-matter simulation of a three-dimensional anomaly. *Physical Review Letters*, 53:2449, 1984.

[31] K. I. Bolotin, K. J. Sikes, J. Hone, H. L. Stormer, and P. Kim. Temperature-dependent transport in suspended graphene. *Physical Review Letters*, 101(9):096802, 2008.

[32] Masaaki Nakamura. Orbital magnetism and transport phenomena in two-dimensional dirac fermions in a weak magnetic field. *Physical Review B*, 76:113301, 2007.

[33] Amit Ghosal, Pallab Goswami, and Sudip Chakravarty. Diamagnetism of nodal fermions. *Physical Review B*, 75:115123, 2007.

[34] Yisong Zheng and Tsuneya Ando. Hall conductivity of a two-dimensional graphite system. *Physical Review B*, 65:245420, 2002.

[35] V. P. Gusynin and S. G. Sharapov. Unconventional integer quantum hall effect in graphene. *Physical Review Letters*, 95:146801, 2005.

[36] N. M. R. Peres, F. Guinea, and A. H. Castro Neto. Electronic properties of disordered two-dimensional carbon. *Physical Review B*, 73:125411, 2006.

[37] Yaping Yang, Yi-Chao Zou, Colin R Woods, Yanmeng Shi, Jun Yin, Shuigang Xu, Servet Ozdemir, Takashi Taniguchi, Kenji Watanabe, Andre K Geim, and others. Stacking order in graphite films controlled by van der Waals technology. *Nano Letters*, 19(12):8526, 2019.

[38] Fabian R. Geisenhof, Felix Winterer, Stefan Wakolbinger, Tobias D. Gokus, Yasin C. Durmaz, Daniela Priesack, Jakob Lenz, Fritz Keilmann, Kenji Watanabe, Takashi Taniguchi, Raúl Guerrero-Avilés, Marta Pelc, Andres Ayuela, and R. Thomas Weitz. Anisotropic strain-induced soliton movement changes stacking order and band structure of graphene multilayers: Implications for charge transport. *ACS Applied Nano Materials*, 2(9):6067, 2019.

[39] J.-C. Charlier, X. Gonze, and J.-P. Michenaud. First-principles study of the stacking effect on the electronic properties of graphite(s). *Carbon*, 32(2):289, 1994.

[40] Abderrezak Torche, Francesco Mauri, Jean-Christophe Charlier, and Matteo Calandra. First-principles determination of the raman fingerprint of rhombohedral graphite. *Physical Review Materials*, 1(4):041001, 2017.

[41] Mikito Koshino. Electronic transmission throughAB-BAdomain boundary in bilayer graphene. *Physical Review B*, 88(11):115409, 2013.

[42] Yuan Cao, Valla Fatemi, Shiang Fang, Kenji Watanabe, Takashi Taniguchi, Efthimios Kaxiras, and Pablo Jarillo-Herrero. Unconventional superconductivity in magic-angle graphene superlattices. *Nature*, 556(7699):43, 2018.

[43] Isabelle Dumé. 'magic-angle graphene' behaves like a high-temperature superconductor. *2D materials*, 2018.

[44] Yang-Zhi Chou, Fengcheng Wu, and Jay D. Sau. Charge density wave and finite-temperature transport in minimally twisted bilayer graphene. *Physical Review B*, 104:045146, 2021.

[45] Erika N. Lima, Tome M. Schmidt, and Ricardo W. Nunes. Topologically protected metallic states induced by a one-dimensional extended defect in the bulk of a 2d topological insulator. *Nano Letters*, 16(7):4025, 2016.

[46] Jayeeta Lahiri, You Lin, Pinar Bozkurt, Ivan I. Oleynik, and Matthias Batzill. An extended defect in graphene as a metallic wire. *Nature Nanotechnology*, 5(5):326, 2010.

[47] Richard M. Martin. *Electronic Structure*. Cambridge University Press, 2004.

[48] John P Perdew and Alex Zunger. Self-interaction correction to density-functional approximations for many-electron systems. *Physical Review B*, 23(10):5048, 1981.

[49] Seymour H Vosko, Leslie Wilk, and Marwan Nusair. Accurate spin-dependent electron liquid correlation energies for local spin density calculations: a critical analysis. *Canadian Journal of physics*, 58(8):1200, 1980.

[50] Frank Herman, John P Van Dyke, and Irene B Ortenburger. Improved statistical exchange approximation for inhomogeneous many-electron systems. *Physical Review Letters*, 22(16):807, 1969.

[51] Takao Tsuneda. *Density Functional Theory in Quantum Chemistry*. Springer Japan, 2014.

[52] J Harris and RO Jones. The surface energy of a bounded electron gas. *Journal of Physics F: Metal Physics*, 4(8):1170, 1974.

[53] LJ Sham. Exchange and correlation in density-functional theory. *Physical Review B*, 32(6):3876, 1985.

[54] Kyuho Lee, Éamonn D. Murray, Lingzhu Kong, Bengt I. Lundqvist, and David C. Langreth. Higher-accuracy van der waals density functional. *Physical Review B*, 82:081101, 2010.

[55] Ikutaro Hamada. van der waals density functional made accurate. *Physical Review B*, 89:121103, 2014.

[56] M. Dion, H. Rydberg, E. Schröder, D. C. Langreth, and B. I. Lundqvist. Van der waals density functional for general geometries. *Physical Review Letters*, 92:246401, 2004.

[57] Per Hyldgaard, Yang Jiao, and Vivekanand Shukla. Screening nature of the van der waals density functional method: A review and analysis of the many-body physics foundation. *Journal of Physics: Condensed Matter*, 32(39):393001, 2020.

[58] Kristian Berland, Valentino R Cooper, Kyuho Lee, Elsebeth Schröder, T Thonhauser, Per Hyldgaard, and Bengt I Lundqvist. van der waals forces in density functional theory: a review of the vdw-df method. *Reports on Progress in Physics*, 78(6):066501, 2015.

[59] David Tománek and Steven G Louie. First-principles calculation of highly asymmetric structure in scanning-tunneling-microscopy images of graphite. *Physical Review B*, 37(14):8327, 1988.

[60] Liyuan Zhang, Yan Zhang, Jorge Camacho, Maxim Khodas, and Igor Zaliznyak. The experimental observation of quantum hall effect

of l=3 chiral quasiparticles in trilayer graphene. *Nature Physics*, 7(12):953, 2011.

[61] Chun Hung Lui, Zhiqiang Li, Zheyuan Chen, Paul V. Klimov, Louis E. Brus, and Tony F. Heinz. Imaging stacking order in few-layer graphene. *Nano Letters*, 11(1):164, 2011.

[62] A C Ferrari, J C Meyer, V Scardaci, C Casiraghi, M Lazzeri, F Mauri, S Piscanec, D Jiang, K S Novoselov, S Roth, and A K Geim. Raman spectrum of graphene and graphene layers. *Physical Review Letters*, 97(18):187401, 2006.

[63] D Graf, F Molitor, K Ensslin, C Stampfer, A Jungen, C Hierold, and L Wirtz. Spatially resolved raman spectroscopy of single- and few-layer graphene. *Nano Letters*, 7(2):238, 2007.

[64] Jonathan S. Alden, Adam W. Tsen, Pinshane Y. Huang, Robert Hovden, Lola Brown, Jiwoong Park, David A. Muller, and Paul L. McEuen. Strain solitons and topological defects in bilayer graphene. *Proceedings of the National Academy of Sciences*, 110(28):11256, 2013.

[65] Wenjing Zhang, Jiaxu Yan, Chang-Hsiao Chen, Liu Lei, Jer-Lai Kuo, Zexiang Shen, and Lain-Jong Li. Molecular adsorption induces the transformation of rhombohedral- to Bernal-stacking order in trilayer graphene. *Nature Communications*, 4(1):2074, 2013.

[66] Masato Aoki and Hiroshi Amawashi. Dependence of band structures on stacking and field in layered graphene. *Solid State Communications*, 142(3):123, 2007.

[67] Natalia Cortés, Oscar Negrete, Francisco J. Peña, and Patricio Vargas. Gate-tunable charge carrier electrocaloric effect in trilayer graphene. *Scientific Reports*, 11(1):1, 2021.

[68] K. S. Novoselov, E. McCann, S. V. Morozov, V. I. Fal'ko, M. I. Katsnelson, U. Zeitler, D. Jiang, F. Schedin, and A. K. Geim. Unconventional quantum hall effect and berry's phase of 2π in bilayer graphene. *Nature Physics*, 2(3):177, 2006.

[69] F. Guinea, A. H. Castro Neto, and N. M. R. Peres. Electronic states and landau levels in graphene stacks. *Physical Review B*, 73(24):245426, 2006.

[70] C. P. Chang, J. Wang, C. L. Lu, Y. C. Huang, M. F. Lin, and R. B. Chen. Optical properties of simple hexagonal and rhombohedral few-layer graphenes in an electric field. *Journal of Applied Physics*, 103(10):103109, 2008.

[71] Changhua Bao, Wei Yao, Eryin Wang, Chaoyu Chen, José Avila, Maria C. Asensio, and Shuyun Zhou. Stacking-dependent electronic structure of trilayer graphene resolved by nanospot angle-resolved photoemission spectroscopy. *Nano Letters*, 17(3):1564, 2017.

[72] Mikito Koshino and Edward McCann. Trigonal warping and berry's phase $n\pi$ in abc-stacked multilayer graphene. *Physical Review B*, 80:165409, 2009.

[73] N. B. Kopnin, T. T. Heikkilä, and G. E. Volovik. High-temperature surface superconductivity in topological flat-band systems. *Physical Review B*, 83(22):220503, 2011.

[74] N. B. Kopnin, M. Ijäs, A. Harju, and T. T. Heikkilä. High-temperature surface superconductivity in rhombohedral graphite. *Physical Review B*, 87(14), 2013.

[75] T. Scheike, W. Böhlmann, P. Esquinazi, J. Barzola-Quiquia, A. Ballestar, and A. Setzer. Can doping graphite trigger room temperature superconductivity? evidence for granular high-temperature superconductivity in water-treated graphite powder. *Advanced Materials*, 24(43):5826, 2012.

[76] Minoru Otani, Yoshiteru Takagi, Mikito Koshino, and Susumu Okada. Phase control of magnetic state of graphite thin films by electric field. *Applied Physics Letters*, 96(24):242504, 2010.

[77] G Kresse and J Hafner. Ab initio molecular dynamics for liquid metals. *Physical Review B*, 47(1):558, 1993.

[78] G Kresse and J Furthmüller. Efficiency of ab-initio total energy calculations for metals and semiconductors using a plane-wave basis set. *Computational Materials Science*, 6(1):15, 1996.

[79] G Kresse and J Furthmüller. Efficient iterative schemes for ab initio total-energy calculations using a plane-wave basis set. *Physical Review B*, 54(16):11169, 1996.

[80] Jiří Klimeš, David R Bowler, and Angelos Michaelides. Van der Waals density functionals applied to solids. *Physical Review B*, 83(19):195131, 2011.

[81] E. Mostaani, N.D. Drummond, and Fal'ko. V. I. Quantum Monte Carlo Calculation of the Binding Energy of Bilayer Graphene. *Physical Review Letters*, 115(11):115501, 2015.

[82] Adolfo De Sanctis, Jake D Mehew, Saad Alkhalifa, Freddie Withers, Monica F Craciun, and Saverio Russo. Strain-engineering of twist-angle in graphene/hBN superlattice devices. *Nano Letters*, 18(12):7919, 2018.

[83] Stefan Wakolbinger, Fabian R Geisenhof, Felix Winterer, Samuel Palmer, Juri G Crimmann, Kenji Watanabe, Takashi Taniguchi, Frank Trixler, and R Thomas Weitz. Locally-triggered hydrophobic collapse induces global interface self-cleaning in van-der-waals heterostructures at room-temperature. *2D Materials*, 7(3):035002, 2020.

[84] Keun Soo Kim, Yue Zhao, Houk Jang, Sang Yoon Lee, Jong Min Kim, Kwang S. Kim, Jong-Hyun Ahn, Philip Kim, Jae-Young Choi, and Byung Hee Hong. Large-scale pattern growth of graphene films for stretchable transparent electrodes. *Nature*, 457(7230):706, 2009.

[85] Lujun Wang, Simon Zihlmann, Andreas Baumgartner, Jan Overbeck, Kenji Watanabe, Takashi Taniguchi, Péter Makk, and Christian Schönenberger. In situ strain tuning in hBN-encapsulated graphene electronic devices. *Nano Letters*, 19(6):4097, 2019.

[86] Tom Vincent, Vishal Panchal, Tim Booth, Stephen R Power, Antti-Pekka Jauho, Vladimir Antonov, and Olga Kazakova. Probing the

nanoscale origin of strain and doping in graphene-hBN heterostructures. *2D Materials*, 6(1):15021, 2018.

[87] Jean Paul Nery, Matteo Calandra, and Francesco Mauri. Ab-initio energetics of graphite and multilayer graphene: stability of Bernal versus rhombohedral stacking. *2D Materials*, 8(3):35006, 2021.

[88] D G Purdie, N M Pugno, T Taniguchi, K Watanabe, A C Ferrari, and A Lombardo. Cleaning interfaces in layered materials heterostructures. *Nat. Commun.*, 9(1):5387, 2018.

[89] W. Bao, L. Jing, J. Velasco, Y. Lee, G. Liu, D. Tran, B. Standley, M. Aykol, S. B. Cronin, D. Smirnov, M. Koshino, E. McCann, M. Bockrath, and C. N. Lau. Stacking-dependent band gap and quantum transport in trilayer graphene. *Nature Physics*, 7(12):948, 2011.

[90] Chun Hung Lui, Zhiqiang Li, Kin Fai Mak, Emmanuele Cappelluti, and Tony F. Heinz. Observation of an electrically tunable band gap in trilayer graphene. *Nature Physics*, 7(12):944, 2011.

[91] Anya L. Grushina, Dong-Keun Ki, Mikito Koshino, Aurelien A. L. Nicolet, Clément Faugeras, Edward McCann, Marek Potemski, and Alberto F. Morpurgo. Insulating state in tetralayers reveals an even–odd interaction effect in multilayer graphene. *Nature Communications*, 6(1):1, 2015.

[92] Y. Lee, D. Tran, K. Myhro, J. Velasco, N. Gillgren, C. N. Lau, Y. Barlas, J. M. Poumirol, D. Smirnov, and F. Guinea. Competition between spontaneous symmetry breaking and single-particle gaps in trilayer graphene. *Nature Communications*, 5(1):1, 2014.

[93] K. Zou, Fan Zhang, C. Clapp, A. H. MacDonald, and J. Zhu. Transport studies of dual-gated ABC and ABA trilayer graphene: Band gap opening and band structure tuning in very large perpendicular electric fields. *Nano Letters*, 13(2):369, 2013.

[94] Lili Jiang, Sheng Wang, Zhiwen Shi, Chenhao Jin, M Iqbal Bakti Utama, Sihan Zhao, Yuen-Ron Shen, Hong-Jun Gao, Guangyu

Zhang, and Feng Wang. Manipulation of domain-wall solitons in bi-and trilayer graphene. *Nature Nanotechnology*, 13(3):204, 2018.

[95] Haiming Zhao, Yung-Chang Lin, Chao-Hui Yeh, He Tian, Yu-Chen Chen, Dan Xie, Yi Yang, Kazu Suenaga, Tian-Ling Ren, and Po-Wen Chiu. Growth and Raman spectra of single-crystal trilayer graphene with different stacking orientations. *ACS Nano*, 8(10):10766, 2014.

[96] Ming Huang, Pavel V. Bakharev, Zhu-Jun Wang, Mandakini Biswal, Zheng Yang, Sunghwan Jin, Bin Wang, Hyo Ju Park, Yunqing Li, Deshun Qu, Youngwoo Kwon, Xianjue Chen, Sun Hwa Lee, Marc-Georg Willinger, Won Jong Yoo, Zonghoon Lee, and Rodney S. Ruoff. Large-area single-crystal AB-bilayer and ABA-trilayer graphene grown on a Cu/Ni (111) foil. *Nature Nanotechnology*, 15(4):289, 2020.

[97] M. Pelc, W. Jaskólski, A. Ayuela, and Leonor Chico. Topologically confined states at corrugations of gated bilayer graphene. *Physical Review B*, 92(8):085433, 2015.

[98] F. Zhang, A. H. MacDonald, and E. J. Mele. Valley chern numbers and boundary modes in gapped bilayer graphene. *Proceedings of the National Academy of Sciences*, 110(26):10546, 2013.

[99] Pablo San-Jose and Elsa Prada. Helical networks in twisted bilayer graphene under interlayer bias. *Physical Review B*, 88(12):121408, 2013.

[100] Shengqiang Huang, Kyounghwan Kim, Dmitry K Efimkin, Timothy Lovorn, Takashi Taniguchi, Kenji Watanabe, Allan H MacDonald, Emanuel Tutuc, and Brian J LeRoy. Topologically protected helical states in minimally twisted bilayer graphene. *Physical Review Letters*, 121(3):037702, 2018.

[101] Pinshane Y. Huang, Carlos S. Ruiz-Vargas, Arend M. van der Zande, William S. Whitney, Mark P. Levendorf, Joshua W. Kevek, Shivank Garg, Jonathan S. Alden, Caleb J. Hustedt, Ye Zhu, Jiwoong Park, Paul L. McEuen, and David A. Muller. Grains and grain

boundaries in single-layer graphene atomic patchwork quilts. *Nature*, 469(7330):389, 2011.

[102] A Ayuela, W Jaskólski, H Santos, and Leonor Chico. Electronic properties of graphene grain boundaries. *New Journal of Physics*, 16(8):083018, 2014.

[103] Juntao Song, Haiwen Liu, Hua Jiang, Qing-feng Sun, and X. C. Xie. One-dimensional quantum channel in a graphene line defect. *Physical Review B*, 86:085437, 2012.

[104] Ting Hu, Jian Zhou, Jinming Dong, and Yoshiyuki Kawazoe. Strain-induced ferromagnetism in zigzag edge graphene nanoribbon with a topological line defect. *Physical Review B*, 86:125420, 2012.

[105] Min Kan, Jian Zhou, Qiang Sun, Qian Wang, Yoshiyuki Kawazoe, and Puru Jena. Tuning magnetic properties of graphene nanoribbons with topological line defects: From antiferromagnetic to ferromagnetic. *Physical Review B*, 85:155450, 2012.

[106] M. Pelc, L. Chico, A. Ayuela, and W. Jaskólski. Grain boundaries with octagonal defects in graphene nanoribbons and nanotubes. *Physical Review B*, 87(16):165427, 2013.

[107] D. A. Bahamon, A. L. C. Pereira, and P. A. Schulz. Third edge for a graphene nanoribbon: A tight-binding model calculation. *Physical Review B*, 83(15):155436, 2011.

[108] Susumu Okada, Kyoko Nakada, Kei Kuwabara, Kota Daigoku, and Takazumi Kawai. Ferromagnetic spin ordering on carbon nanotubes with topological line defects. *Physical Review B*, 74(12):121412, 2006.

[109] Jing Li, Ke Wang, Kenton J McFaul, Zachary Zern, Yafei Ren, Kenji Watanabe, Takashi Taniguchi, Zhenhua Qiao, and Jun Zhu. Gate-controlled topological conducting channels in bilayer graphene. *Nature Nanotechnology*, 11(12):1060, 2016.

[110] W Jaskólski, M Pelc, Garnett W Bryant, Leonor Chico, and A Ayuela. Controlling the layer localization of gapless states in

bilayer graphene with a gate voltage. *2D Materials*, 5(2):025006, 2018.

[111] Abolhassan Vaezi, Yufeng Liang, Darryl H. Ngai, Li Yang, and Eun-Ah Kim. Topological edge states at a tilt boundary in gated multilayer graphene. *Physical Review X*, 3:021018, 2013.

[112] Long Ju, Zhiwen Shi, Nityan Nair, Yinchuan Lv, Chenhao Jin, Jairo Velasco, Claudia Ojeda-Aristizabal, Hans A. Bechtel, Michael C. Martin, Alex Zettl, James Analytis, and Feng Wang. Topological valley transport at bilayer graphene domain walls. *Nature*, 520(7549):650, 2015.

[113] Ivar Martin, Ya. M. Blanter, and A. F. Morpurgo. Topological confinement in bilayer graphene. *Physical Review Letters*, 100(3):036804, 2008.

[114] Hao Chen, Pinjia Zhou, Jiawei Liu, Jiabin Qiao, Barbaros Oezyilmaz, and Jens Martin. Gate controlled valley polarizer in bilayer graphene. *Nature Communications*, 11(1):1, 2020.

[115] W. Jaskólski, M. Pelc, Leonor Chico, and A. Ayuela. Existence of nontrivial topologically protected states at grain boundaries in bilayer graphene: signatures and electrical switching. *Nanoscale*, 8:6079, 2016.

[116] D.J. Klein. Graphitic polymer strips with edge states. *Chemical Physics Letters*, 217(3):261, 1994.

[117] W. Jaskólski and A. Ayuela. Spin-layer locked gapless states in gated bilayer graphene. *RSC Advances*, 9(72):42140, 2019.

[118] José M Soler, Emilio Artacho, Julian D Gale, Alberto García, Javier Junquera, Pablo Ordejón, and Daniel Sánchez-Portal. The SIESTA method for ab initio order-n materials simulation. *Journal of Physics: Condensed Matter*, 14(11):2745, 2002.

[119] Jiří Klimeš, David R Bowler, and Angelos Michaelides. Chemical accuracy for the van der waals density functional. *J. Phys. Condens. Matter*, 22(2):022201, 2009.

[120] G. Grüner. The dynamics of charge-density waves. *Reviews of Modern Physics*, 60(4):1129, 1988.

[121] G Buchs, M Marganska, JW González, K Eimre, CA Pignedoli, D Passerone, Andrés Ayuela, O Gröning, and Dario Bercioux. Metallic carbon nanotube quantum dots with broken symmetries as a platform for tunable terahertz detection. *Applied Physics Reviews*, 8(2):021406, 2021.

[122] Seong-Jun Yang, Min-Yeong Choi, and Cheol-Joo Kim. Engineering grain boundaries in two-dimensional electronic materials. *Advanced Materials*, page 2203425, 2022.

[123] Stefan Grimme. Semiempirical gga-type density functional constructed with a long-range dispersion correction. *Journal of Computational Chemistry*, 27(15):1787, 2006.

[124] Stefan Grimme, Jens Antony, Stephan Ehrlich, and Helge Krieg. A consistent and accurate ab initio parametrization of density functional dispersion correction (dft-d) for the 94 elements h-pu. *The Journal of Chemical Physics*, 132(15):154104, 2010.

[125] Stefan Grimme, Stephan Ehrlich, and Lars Goerigk. Effect of the damping function in dispersion corrected density functional theory. *Journal of Computational Chemistry*, 32(7):1456, 2011.

[126] Guillermo Román-Pérez and José M Soler. Efficient implementation of a van der waals density functional: application to double-wall carbon nanotubes. *Physical Review Letters*, 103(9):096102, 2009.

[127] N. David Mermin. Thermal properties of the inhomogeneous electron gas. *Physical Review*, 137(5A):A1441, 1965.

[128] Yingkai Zhang and Weitao Yang. Comment on "generalized gradient approximation made simple". *Physical Review Letters*, 80(4):890, 1998.

[129] Irina V Lebedeva, Alexander V Lebedev, Andrey M Popov, and Andrey A Knizhnik. Comparison of performance of van der waals-corrected exchange-correlation functionals for interlayer interaction

in graphene and hexagonal boron nitride. *Computational Materials Science*, 128:45, 2017.

[130] Fabien Tran, Leila Kalantari, Boubacar Traoré, Xavier Rocquefelte, and Peter Blaha. Nonlocal van der waals functionals for solids: Choosing an appropriate one. *Physical Review Materials*, 3:063602, 2019.

[131] Torbjörn Björkman. Testing several recent van der waals density functionals for layered structures. *The Journal of Chemical Physics*, 141(7):074708, 2014.

[132] Shuigang Xu, Mohammed M. Al Ezzi, Nilanthy Balakrishnan, Aitor Garcia-Ruiz, Bonnie Tsim, Ciaran Mullan, Julien Barrier, Na Xin, Benjamin A. Piot, Takashi Taniguchi, Kenji Watanabe, Alexandra Carvalho, Artem Mishchenko, A. K. Geim, Vladimir I. Fal'ko, Shaffique Adam, Antonio Helio Castro Neto, Kostya S. Novoselov, and Yanmeng Shi. Tunable van hove singularities and correlated states in twisted monolayer–bilayer graphene. *Nature Physics*, 17(5):619, 2021.

[133] Hendrik J. Monkhorst and James D. Pack. Special points for brillouin-zone integrations. *Physical Review B*, 13:5188, 1976.